

INFRARED EJECTA AND COLD DUST IN THE YOUNG SUPERNOVA REMNANT N132D

JEONGHEE RHO¹, ARAVIND P. RAVI², JONATHAN D. SLAVIN³ HEECHAN CHA^{4, 5}

Draft version March 10, 2023

ABSTRACT

We present *Spitzer*, *WISE*, and *Herschel* observations of the young supernova remnant (SNR) N132D in the LMC, including 3-40 μm *Spitzer* IRS mapping, 12 μm *WISE* and 70, 100, 160, 250, 350, and 500 μm *Herschel* images. The high-velocity lines of [Ne II] at 12.8 μm , [Ne III] at 15.5 μm , and [O IV] 26 μm reveal infrared ejecta concentrated in a central ring and coincide the optical and X-ray ejecta. *Herschel* images reveal far-IR emission coinciding with the central ejecta, which suggests that the IR emission is freshly formed, cold dust in the SN-ejecta. The infrared spectra are remarkably similar to those of another young SNR of 1E0102 with Ne and O lines. Shock modeling of the Ne ejecta emission suggests a gas temperature of 300 - 600 K and densities in the range $1000 - 2 \times 10^4 \text{ cm}^{-3}$ in the post-shock photoionized region. The IR continuum from the ejecta shows an 18 μm -peak dust feature. We performed spectral fitting to the IRS dust continuum and *Herschel* photometry. The dust mass associated with the central ejecta is $1.25 \pm 0.65 M_{\odot}$, while the 18 μm dust feature requires forsterite grains. The dust mass of the central ejecta region in N132D is higher than those of other young SNRs, which is likely associated with its higher progenitor mass. We discuss the dust productivity in the ejecta of N132D and infer its plausible implications for the dust in the early Universe.

1. INTRODUCTION

Core-collapse supernovae (ccSN) are the catastrophic deaths of massive stars. The most direct method of probing the nuclear physics that takes place in ccSNe is to examine their nucleosynthetic products and to constrain the explosion mechanism by observing their supernova remnants (SNRs). Dust formation in ccSNe, e.g. Types II, Ib and Ic, may account for the presence of large amounts of dust observed in high- z galaxies, since their progenitors, stars much more massive than the sun, evolve on much shorter timescales (millions to a few tens of millions of years) than the other main source of dust in the current Universe, asymptotic giant branch stars, and can eject large amounts of heavy elements into the ISM. If a typical Type II SN were able to condense only 10% of its heavy elements into dust grains, it could eject around half a solar mass of dust into the ISM. The predicted dust mass formed in a ccSN depends on its progenitor mass; for a progenitor mass of 15 to 30 M_{\odot} , the predicted dust mass ranges from 0.1 to 1.0 M_{\odot} (Nozawa et al. 2003; Todini & Ferrara 2001). For a star formation rate (SFR) 100 times that of the Milky Way this would lead to a dust mass of order $10^8 M_{\odot}$ at $z = 6.3\text{--}7.5$ (Nozawa et al. 2003; Michałowski 2015).

Herschel and *Spitzer* observations of four SNRs: Cas A (Rho et al. 2008; De Looze et al. 2017), SN 1987A (Matsuura et al. 2011, 2015), the Crab Nebula (Gomez et al. 2012), and G54.1+0.3 (Rho et al. 2018; Temim et al. 2017) yielded significant amounts of dust (0.1-1 M_{\odot} per

SN). The longer wavelength far-infrared and submillimeter (FIR-submm) observations for G54.1+0.3 revealed a cooler component of dust at $\sim 35 \text{ K}$, and the Photodetector Array Camera (PACS) and the Spectral and Photometric Imaging Receiver (SPIRE) images show ejecta emission. Both Cas A and G54.1+0.3 show 21 and 11 μm dust features which are attributed to silica (SiO_2) and SiC, respectively (Rho et al. 2018). De Looze et al. (2017) performed a spatially resolved analysis of ISM and SN dust emission using 17 - 500 μm maps that allowed them to exclude the ISM contribution. The derived dust masses for both SN were between 0.4 and 0.6 M_{\odot} . *Herschel* observations reveal significant quantities of cool dust (at 20-50 K) with masses of 0.1-0.65 M_{\odot} in the pulsar-wind nebulae of G11.2-0.3, G21.5-0.9, and G29.7-0.3 (Chawner et al. 2019) and MSH 15-52 (G320.4-1.2, Millard et al. 2021). The dust masses of the eight young SNRs (YSNRs) observed with *Herschel* and *Spitzer* exceed by an order of magnitude the previously detected dust masses and are two orders of magnitude higher than those observed in SNe (Kotak et al. 2006; Gall et al. 2011). They also are in agreement with theoretical models of dust condensation (Nozawa et al. 2003; Todini & Ferrara 2001; Sluder et al. 2018). These results support the theory that the huge quantities of SN-dust in high-redshift galaxies are produced in ccSNe (Isaak et al. 2002; Laporte et al. 2017; Spilker et al. 2018; Dayal et al. 2022; Tacchella et al. 2022; Sommovigo et al. 2022).

Despite this evidence that large amounts of dust are created in ccSNe, uncertainties remain about the contribution of dust by such SNe to the ISM. The cold dust observed in young remnants is generally in the interior of the remnants (see De Looze et al. 2017) and has not yet encountered the reverse shock, which will eventually propagate to the center of the remnant. The amount of dust destruction, once the shock hits the dense clumps of ejecta, depends on a variety of parameters such as the grain size distribution, the grain material, and the density contrast between the clumps and lower density

¹ SETI Institute, 189 N. Bernardo Ave., Mountain View, CA 94043; jrho@seti.org

² Department of Physics, University of Texas at Arlington, Box 19059, Arlington, TX 76019, USA

³ Center for Astrophysics | Harvard & Smithsonian, 60 Garden Street, Cambridge, MA 02138, USA

⁴ Department of Physics and Astronomy, University of Texas at San Antonio, San Antonio, TX 78249, USA

⁵ Department of Astronomy and Space Science, Chungbuk National University, Cheongju, 28644, Republic of Korea

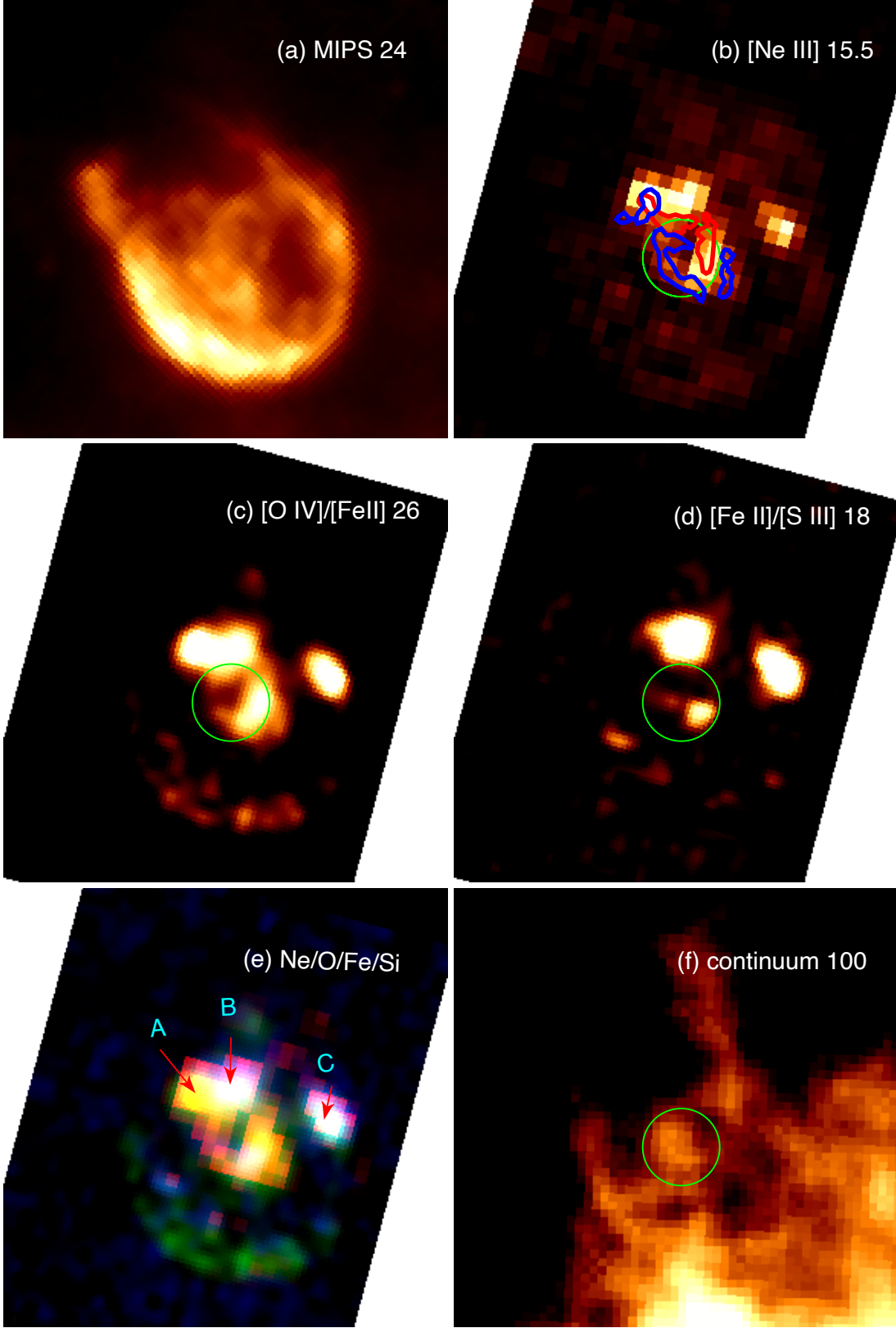


FIG. 1.— *Spitzer* and *Herschel* images of N132D: (a) MIPS 24 μm ; (b) [Ne III] 15.5 μm ; (c) [O IV]/[Fe II] 26 μm (indicating [O IV] at 25.89 μm and/or [Fe II] at 25.98 μm and the IRS spectrum implies that the emission is mainly from [O IV] as shown in Fig. 2), which coincides optical ejecta (contours are marked in green); (d) [Fe II]/[S III] ([Fe II] 17.9 μm and/or [S III] at 18.7 μm ; (e) three color images of ejecta (red, green, and blue representing [Ne III], [O IV]/[Fe II], [Fe II]/[Si II], respectively); (f) *Herschel* 100 μm . In b, c, d, and f the central emission is denoted by green circles. The optical [O III] (5007 Å) ejecta (Morse et al. 1995) of blue-shifted (in cyan) and red-shifted (in red) ejecta are marked in the [Ne III] image (b). In panel (e), regions of northeastern ejecta, Lasker’s Bowl, and West Complex are marked as “A”, “B” and “C”, respectively. The images are centered on R.A. 5^h25^m03.23^s and Dec. -69+°38′24.43″ (J2000) with each field of view (FOV) of 2.84′x2.84′. The north is up, and the east is to the left; all other images have the same direction.

ejecta as well as the shock speed (Silvia et al. 2012; Kirchschlager et al. 2019). Because the dust formed in ccSNe includes sufficiently large grains ($0.1 - 0.5 \mu\text{m}$), a significant fraction of the grains can survive (10 - 20% for silicate dust and 30 - 50% for carbon dust; Slavin et al. 2020).

Theoretical estimates of the destruction range between almost total to high surviving fractions (Kirchschlager et al. 2019 and references therein). Observational estimates from Cas A for areas of the remnant where the newly-formed dust has already encountered the shock suggest a significant mass of dust can survive into the interstellar medium (De Looze et al. 2017; Priestley et al. 2022).

N132D (SNR B0525-69.6 or SNR J052501-693842) is one of the young SNRs in the Large Magellanic Cloud (LMC) with a diameter of $100''$ (physical size of 25 pc) and age of ~ 2500 (1300 - 3500) yr (Law et al. 2020; Sutherland & Dopita 1995; Lasker 1980; Morse et al. 1995). Despite its age, N132D shows its youth via ejecta emission in its central region. Optical observations identified O-rich ejecta emission (as in Cas A), an inner ring morphology which shows elevated metal abundances, and red and blue-shifted oxygen-rich ejecta with velocities as high as 4400 km s^{-1} (Morse et al. 1995, see blue- and red-contours in Fig. 1b). The SNR's 3-D structures of optical emission observed by the 2.3m telescope at Siding Spring Observatory show that the majority of the ejecta emission comes from a ring of diameter ~ 12 pc (Vogt & Dopita 2011). The 3-D kinematic reconstruction of the optically-emitting, oxygen-rich ejecta observed by the 6.5m Magellan telescope shows a torus-like geometry (Law et al. 2020). Analysis of both the optical and X-ray emission (Borkowski et al. 2007; Hwang et al. 1993) has shown that the ejecta are oxygen-rich. N132D has been classified as a type Ib SNR and its progenitor has been suggested to be a Wolf-Rayet (W/O) star with a mass between 30 and 35 M_{\odot} (Blair et al. 2000). The X-ray observations identified highly ionized oxygen ejecta (Borkowski et al. 2007). K-shell Fe emission in X-rays is detected at the center, and X-ray oxygen emission is detected from the NE ejecta knots (see Figure 1) and at the center (Behar et al. 2001).

The shell emission of N132D is bright in the south-east, where the dominant contributor is the shocked ISM (Blair et al. 2000). Our previous *Spitzer* observations toward the southeastern shell revealed a plateau of polycyclic aromatic hydrocarbon (PAH) emission at $15\text{--}20 \mu\text{m}$, which is due to PAHs with a relatively large number of carbon atoms (Tappe et al. 2006, 2012). The results suggest that PAH molecules in the surrounding medium are swept up and processed in the hot gas of the blast wave shock, where they survive the harsh conditions long enough to be detected.

In this paper, we use archival *Herschel*, *WISE*, and *Spitzer* images and *Spitzer* Infrared Spectrograph (IRS) observations of N132D and present maps of infrared emission from the IR ejecta in the YSNR N132D and the cold dust likely associated with the IR ejecta. The *Herschel* and *WISE* observations of N132D are presented here for the first time. We present dynamic and physical properties of IR ejecta, including shock modeling (Sections 3.1 – 3.2 and 4.1 – 4.3). The *Herschel* images reveal emission from a cold blob that appears at the remnant's

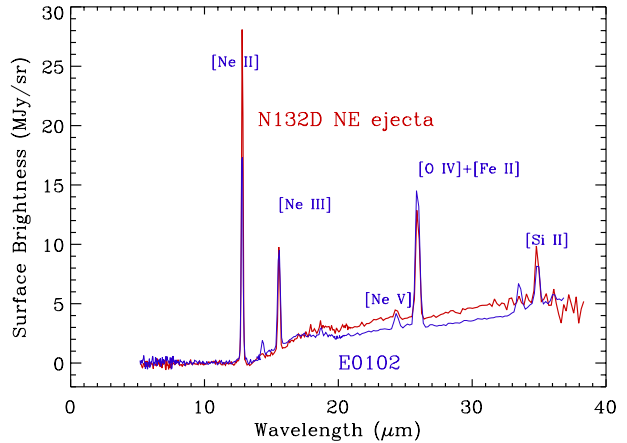


FIG. 2.— *Spitzer* IRS spectrum of N132D (in red) toward NE ejecta (marked ‘A’ in Figure 1e) is compared with that of 1E0102 ejecta emission (in blue; Figure 3 of Rho et al. 2009), showing remarkably similar line strengths and dust continuum shapes. One major difference is the strength of the [Ne II] line, resulting in the different ratio of [Ne II] to [Ne III].

center and coincides with the IR/optical ejecta (Sections 3.3 – 3.4). We estimate the dust mass of the cold blob using *Herschel* and *Spitzer* spectral energy distributions (SEDs; Sections 3.4 and 4.5 – 4.7). We find that the dust mass associated with the ejecta of N132D is higher than those of other young SNRs and its implications for the dust in the early Universe (Section 4.7 for details).

2. OBSERVATIONS

2.1. *Herschel* observations

Herschel observations of N132D were taken as a part of *Herschel* Large Magellanic Cloud (LMC) GTO and Key project (Proposal ID of KPOT_mmeixner.1 and SDP_mmeixner.1) to cover the entire LMC with the *Herschel* Photodetector Array Camera (PACS; Poglitsch et al. 2010) and Spectral and Photometric Imaging Receiver (SPIRE) images using the parallel mode. The observational IDs are 1342187188, 1342195707, 1342195708, 1342202224, and 1342202225. We have used both UPDP (User Provided Data Products) and HPDP (highly-processed data products) and cross-checked the photometry between them. The flux calibration uncertainty for PACS is less than 10% (Poglitsch et al. 2010) and the expected color corrections are small compared to the calibration errors. We, therefore, adopt a 10% calibration error for the 100 and $160 \mu\text{m}$ data. The SPIRE calibration methods and accuracy are outlined by Swinyard et al. (2010) and are estimated to be 7%. The spatial resolutions of *Herschel* images (Fig. 6) are $8''$, $12''$, $18.1''$, $24.9''$ and $36.4''$ at 100, 160, 250, 350 and $500 \mu\text{m}$, respectively. *Herschel* observations of N132D have not been previously published. They enable us to access the coldest dust component, which typically makes up most of the dust mass in SNRs (Gomez et al. 2012; De Looze et al. 2017).

2.2. *WISE* Observations

We used archival Wide-field Infrared Survey Explorer (*WISE*) images of N132D. *WISE* is a whole sky mid-IR survey that uniquely provides data beyond the Galactic plane (Wright et al. 2010). *WISE* $w1$, $w2$, $w3$, and $w4$

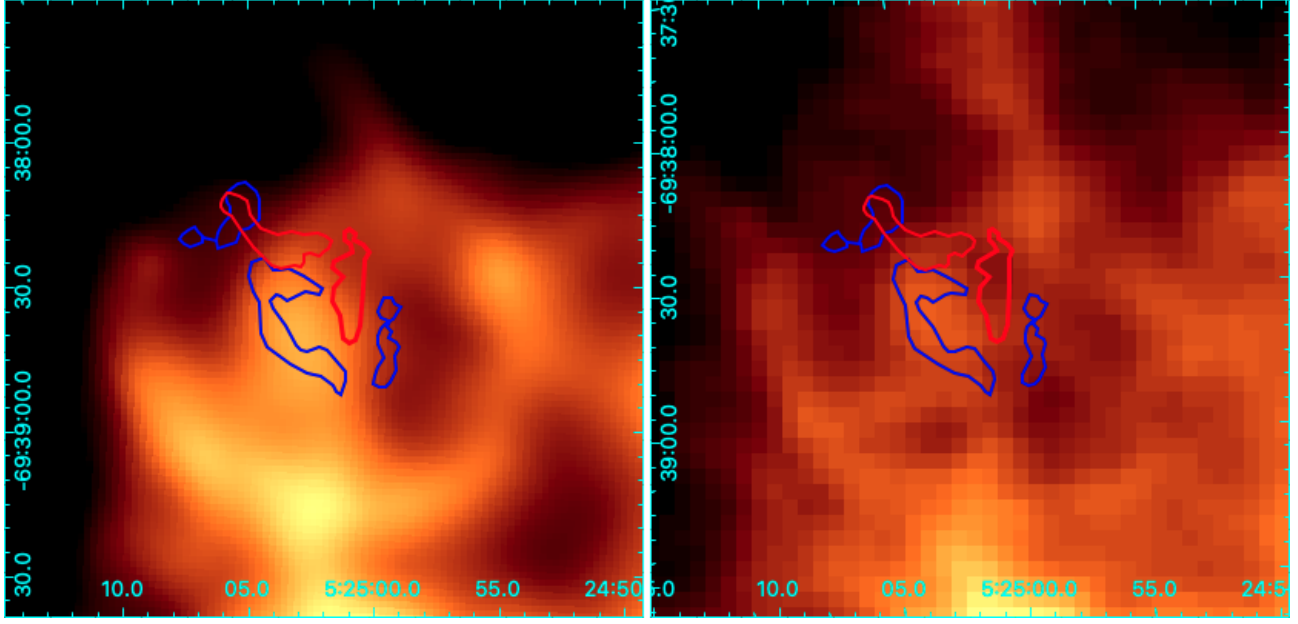


FIG. 3.— *WISE* 12 μm (band 3: *w3*) (left) and *Herschel* 100 μm (right) images of N132D. Both show central emission as well as circular shell-like emission. The optical [O III] (5007 Å) ejecta of blue-shifted (in blue) and red-shifted (in red) ejecta are superposed. The eastern red-shifted ejecta coincides with the *WISE* 12 μm and *Herschel* 100 μm emission.

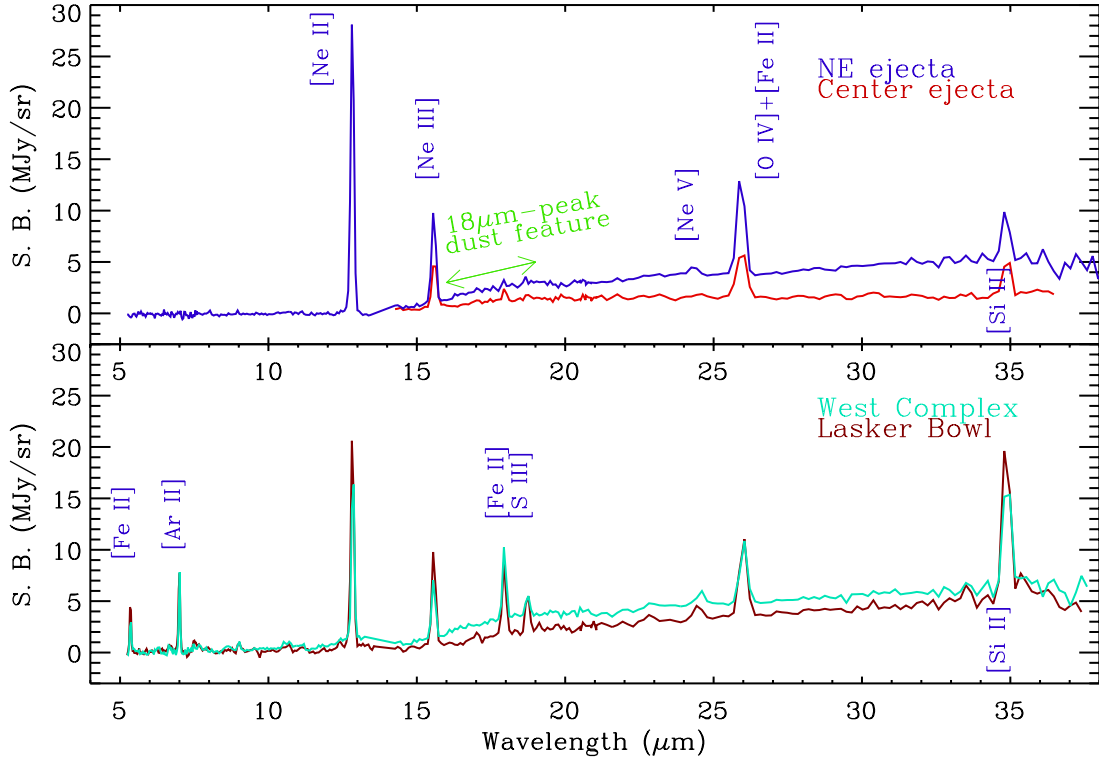


FIG. 4.— Comparison of *Spitzer* IRS spectra (y-axis unit is Surface Brightness) of N132D toward NE Ejecta (the 18 μm -peak dust feature is marked), Lasker's Bowl (marked as 'B' in Figure 1e), West Complex ('C'), and the central ejecta (marked as a circle in Figure 1f; see Section 3.3 for details). The spectrum of the central ejecta in N132D has only long-wavelength ($>15\mu\text{m}$) coverage. The ejecta spectra are dominated by O and Ne lines, Lasker's Bowl and West Complex from the CSM/ISM dense knots include Fe, Ar, and S lines. The position of NE ejecta (marked as 'A' in Figure 1e) is at R. A. $05^{\text{h}}25^{\text{m}}05.62^{\text{s}}$ and Dec. $-69^{\circ}38'12.79''$ (N132D-P3 in the HST spectroscopy observations Blair et al. (2000)), and the center of ejecta is at R. A. $05^{\text{h}}25^{\text{m}}02.03^{\text{s}}$ and Dec. $-69^{\circ}38'44.8''$ (approximate position is N132D-P2 in Blair et al. (2000)). Lasker's Bowl is R. A. $05^{\text{h}}25^{\text{m}}02.40^{\text{s}}$ and Dec. $-69^{\circ}38'12.7''$, J2000) and West Complex is at R. A. $05^{\text{h}}24^{\text{m}}55.15^{\text{s}}$ and Dec. $-69^{\circ}38'26.5''$.

images are centered at 3.4, 4.6, 12, and 22 μm , respectively. Unique to the *WISE* (i.e., not covered by *Spitzer* (3.4, 4.6, and 24 μm), is its broad-band filter (*w3*) centered at 12 μm . The observational parameters are listed in Table 1. *WISE w1* and *w2* images did not detect IR emission from N132D. The *WISE w3* image of N132D is shown in Figure 3, showing the central ejecta emission as well as the circular shell emission. The *WISE w4* image is similar to *Spitzer* 24 μm image but 3 times lower spatial resolution.

2.3. *Spitzer* Observations

We used archival observations (PID of 3483 and 30372) by *Spitzer* for IRS Long-Low (IRS-LL) mapping covering the entire SNR, and IRS staring of Short-Low (SL) observations toward 4 positions (see Tappe et al. 2006). The staring mode was 12 cycles of 60 s exposures for SL. IRS-LL mapping is 2 cycles of 30 s exposure for 10'' stepsize, resulting in 4 minutes of integration per position. The observations are summarized in Table 1. The images and spectra are shown in Figures 1 - 4. We used *Spitzer* IRS spectra of ejecta emission to construct the spectral energy distribution (SED) by combining them with the *Herschel* photometry. Spectral model fitting of dust emission have not been performed and analyzed previously. Note, however, that Tappe et al. (2006, 2012) presented the shocked ISM emission from the southeastern shell and studied its PAH emission.

3. RESULTS

3.1. Infrared Images and Spectra

Figure 1 shows *Spitzer* and *Herschel* images of N132D. Figure 2 is the *Spitzer* IRS spectrum of N132D at the location of the NE ejecta (marked as “A” in Fig. 1e) and shows bright lines of [Ne II] (12.8 μm), [Ne III] (15.5 μm), [O IV] and/or [Fe II] (26 μm), weak lines of [Ne V] (14.3 μm), [Ne V] (24.3 μm), and [Ne III] (36 μm), and possibly [S II] (33.5 μm), and [Si II] (34.89 μm). The O and Ne lines dominate the IR spectrum of N132D, as they do in the optical ejecta (P3 position in Blair et al. 2000) and the X-ray ejecta (green emission in Fig. 2 of Borkowski et al. 2007). The spectrum of N132D and that of the 1E0102 ejecta are compared in Figure 2. The spectra of the two SNRs are remarkably similar in their lines of Ne and O and their continuum shapes, indicating that the N132D emission in the NE position is also likely from the SN ejecta as it is in the case of 1E0102 (Rho et al. 2009). The line intensity ratio between [Ne II] and [Ne III] is much higher in N132D than in 1E0102, indicating that Ne is less ionized in N132D (see Sections 4.1 and 4.3 for discussion).

From the *Spitzer* IRS spectral cube, we generate line maps of [Ne III] at 15.5 μm , [O IV] at 26 μm , and [Si II] at 34.8 μm and present them in Figure 1(b-e). The three line maps each show strong emission at the center with the morphology of a central ring. The [Ne III] and [O IV] emission coincides with the known optical ejecta (see Fig. 1b), including NE ejecta and the central, bright far-IR emission (marked as a circle in Fig. 1f). Figure 3 shows *WISE* 12 μm image, which is essentially a [Ne II] map since [Ne II] (12.8 μm) dominates the emission in the *w3* band. The central emission in the *WISE* image coincides with that of the *Herschel* 100 μm image. The

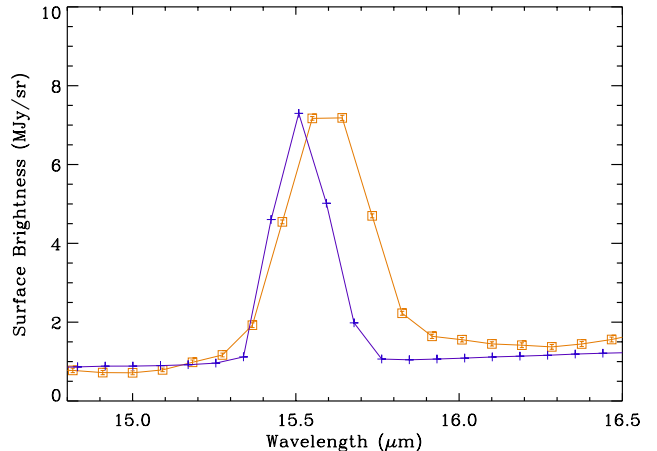


FIG. 5.— Spectral line profile of [Ne III] toward the central ejecta (in orange) compared with the unresolved line profile of Planetary Nebula (PN) NGC6543 (in blue).

CSM/ISM knots of Lasker’s Bowl and the West Complex (marked as ‘B’ and ‘C’ in Figure 1e) produce Fe/Si line emission as well as the Ne and O lines. The Fe/Si emission (from the CSM/ISM knots) at the center (the southwestern part of the circled region in Figure 1d) is anti-correlated with the continuum emission at 100 μm (eastern part of the circled region of Fig. 1f).

IRS spectra at four locations in N132D are compared in Figure 4. The lines of [Ne II] at 12 μm and [O IV]+[Fe II] (likely dominated by [O IV]) in the NE ejecta spectrum are stronger than the CSM/ISM lines at the “Lasker Bowl” and the “West Complex”. The detected lines and their brightnesses are summarized in Table 2. We measured the line brightnesses using two methods: Gaussian fitting and numerical integration of line fluxes over their wavelength ranges. The latter is required in order to account for red- and blue-shifted velocity dispersions. We made extinction corrections using the LMC extinction curve (Fitzpatrick 1985) and assuming $E(B-V) = 0.12$ (Blair et al. 2000), which is equivalent to an interstellar atomic column density of $8 \times 10^{20} \text{ cm}^{-2}$. We then fitted the continuum excluding the wavelengths with ionic lines. Distinct infrared emission is observed from the ejecta and the shock-heated interstellar material.

3.2. Ejecta Lines

We compare the line widths of [Ne II] at 12.8 μm and [Ne III] at 15.57 μm in Table 3. The widths of [Ne II] and [Ne III] are higher than the instrumental spectral width (Houck et al. 2004). The instrument line width of [Ne II] is 0.11 - 0.12 μm ($2340 - 2800 \text{ km s}^{-1}$)¹ from the measurements of the [Ne II] calibration sources of G333.9, NGC6720, and NGC7293 (see also Smith et al. 2007; Rho et al. 2009; Lai et al. 2020). The [Ne II] line width from the NE ejecta is ~ 10 (7 - 27) % broader than the instrument line profile. After taking into account the instrument spectral resolution, we can estimate the true velocity dispersion of [Ne II] line for each position (Table 3). The NE ejecta shows the true velocity dispersion of $1513 \pm 91 \text{ km s}^{-1}$ higher than those (720 - 1120 km s^{-1}) of Lasker’s Bowl and West Complex positions. From the [Ne III] lines, the ejecta (NE and center) show

¹ <https://irsa.ipac.caltech.edu/data/SPITZER/docs/irs/>

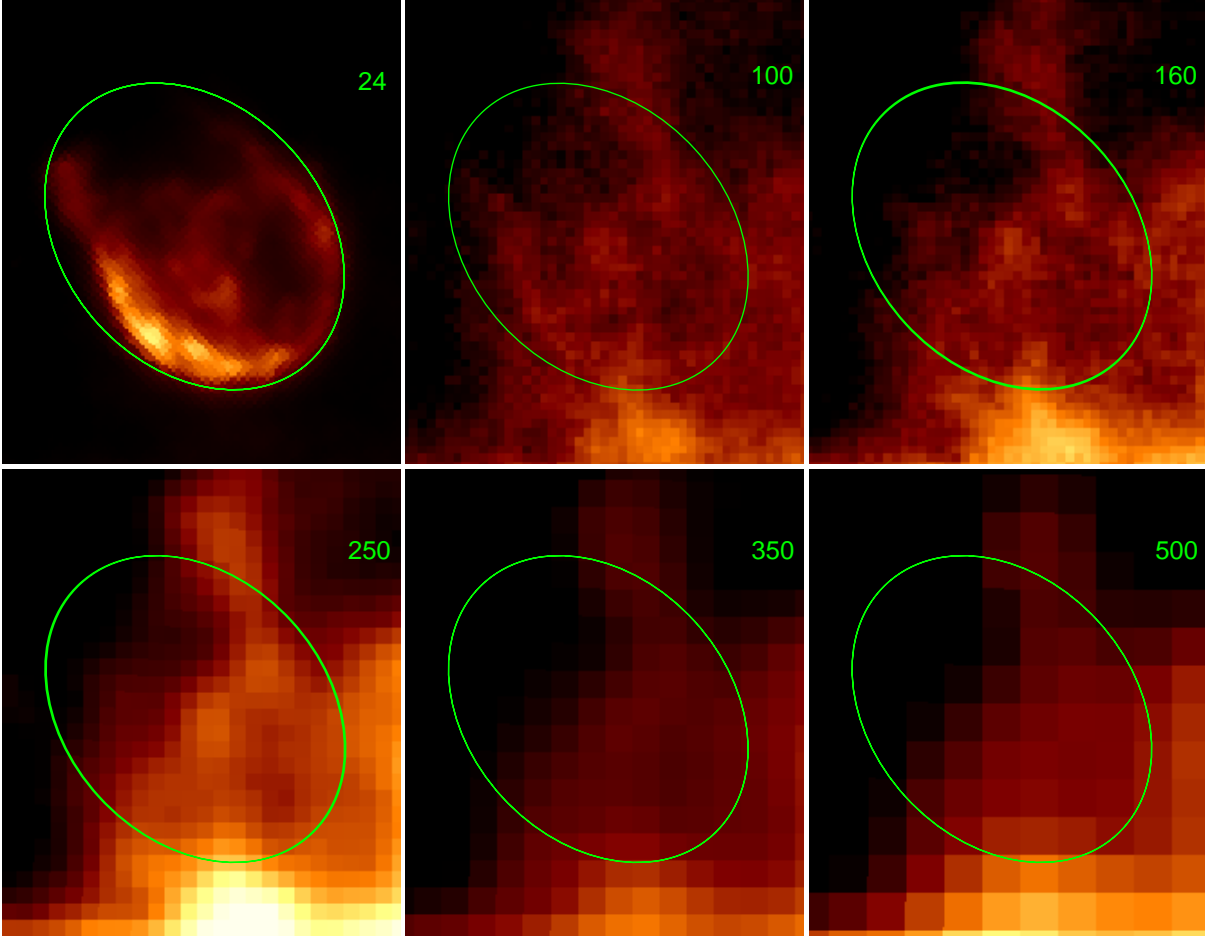


FIG. 6.— *Spitzer* and *Herschel* images towards the SNR N132D with the wavelength in μm unit: *Spitzer* 24 μm (a), *Herschel* PACS 100 μm (b), *Herschel* PACS 160 μm (c), *Herschel* SPIRE 250 μm (d), *Herschel* SPIRE 350 μm (e), *Herschel* SPIRE 500 μm (f) where the wavelength of each image is labeled. The central ejecta blobs (marked as a circle or ellipse in Figures 1 and 9) are detected from 24 to 350 μm , demonstrating the presence of both warm and cold dust; interpretation of the 500 μm image is unclear due to low angular resolution. The image is centered on R.A. $5^{\text{h}}25^{\text{m}}03.16^{\text{s}}$ and Dec. $-69^{\circ}38'24.13''$ (J2000) with a FOV of $2.35' \times 2.89'$.

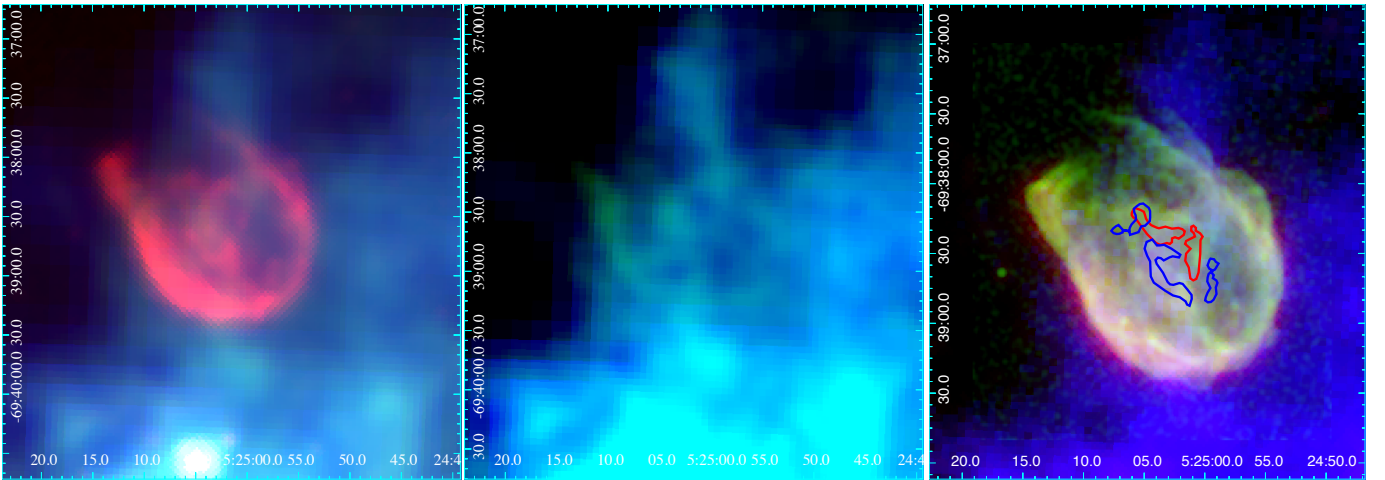


FIG. 7.— Superimposed *Spitzer* and *Herschel* images of SNR N132D: (Left: a) red, green, and blue represent *Spitzer* 24 μm , *Herschel* PACS 100 μm , and *Herschel* SPIRE 350 μm , respectively. (Middle: b) same images as (a) but without the 24 μm image. The SNR and the central blob appear brighter at 100 μm emission (green) than at 350 μm (blue). (Right: c) Multi-wavelength three-color image of N132D at *Herschel* 350 μm (blue), *Spitzer* 24 μm (red), and *Chandra* X-rays (green). The high-velocity blue- and red-shifted optical ejecta are shown as contours (blue and red, respectively).

the true velocity dispersion of $1610 - 1660 \text{ km s}^{-1}$ higher than those ($1260 - 1390 \text{ km s}^{-1}$) of Lasker’s Bowl and West Complex positions. The [Ne III] line width in the central ejecta is $3620 \pm 47 \text{ km s}^{-1}$. Figure 5 shows the line profile of the central ejecta is broader than that of the planetary nebula NGC 6543. The IRS calibration shows the resolving power at $15.55 \mu\text{m}$ is 110, equivalent to a width of $0.14 \mu\text{m}$, equivalent to $\sim 2730 \text{ km s}^{-1}$ (Smith et al. 2007). The width of [Ne III] line of the central ejecta is $3620 \pm 47 \text{ km s}^{-1}$ (see Table 3), and it is $\sim 30\%$ broader than the instrument line profile. The broad line is evidence that the Ne line emission is from SN-ejecta.

The infrared ejecta emission is mainly clustered at the central, inner shell where the optical ejecta are present (see Figures 1b, 1c and 1e). The IRS spectrum of NE ejecta shows strong O and Ne line emission with $18 \mu\text{m}$ -peak dust feature, which is a broad bump between 16 and $19 \mu\text{m}$ as shown in Figure 4 (see also Figure 10 in y-log scale). The infrared emission (central and NE ejecta) coincides with the optical ejecta positions at the center (around the blue-shifted region of B2; Morse et al. 1995; Law et al. 2020) and NE ejecta (B4 in Morse et al. (1995) and N132D-P3 in Blair et al. (2000)). The O and Ne lines are dominant in the optical ejecta (see Table 9 of Blair et al. 2000) as well as in the infrared.

3.3. Cold Dust in the SN ejecta

Figure 6 shows *Herschel* images at $100, 160, 250, 350,$ and $500 \mu\text{m}$ compared with the *Spitzer* MIPS $24 \mu\text{m}$ image (Tappe et al. 2006). N132D has both ejecta emission and a shell of ISM emission. The far-IR maps show cold clouds in the south of the SNR. The PACS and SPIRE images contain infrared (e.g., at $100 \mu\text{m}$ as shown in Fig. 1f) and submm emission at the center of the SNR, which coincides with the optical/infrared ejecta as shown in Figure 1. Figure 7 shows that N132D is bright at *Spitzer* MIPS $24 \mu\text{m}$ (in red in Figure 7a) and that the SNR including the central blob is brighter at $100 \mu\text{m}$ than the $350 \mu\text{m}$ (greener emission from nearby infrared cirrus in Figure 7b). It indicates that N132D, including the central blob, has a hotter temperature than the surrounding cirrus clouds. The SED of the central blob peaks between 100 and $160 \mu\text{m}$ (see Fig. 16). Fits to the SED yield a dust temperature (T_d) of the central blob of $23 - 26 \text{ K}$ (see Table 6), which is hotter than the temperatures of infrared cirrus and ISM clouds ($15 - 20 \text{ K}$; Reach et al. 1995; Boulanger et al. 1996; Lagache et al. 1998; Millard et al. 2021). Details are given in Sections 3.4 and 4.5. In contrast, the shock-heated ISM dust in the southeastern shell of N132D has $T_d = 110 \text{ K}$ and 58 K (Tappe et al. 2006). The lower temperature component ($T_d = 58 \text{ K}$) is much hotter than the dust temperature ($T_d = 23 - 26 \text{ K}$) in the central blob.

Figure 8 compares the *Herschel* $100 \mu\text{m}$ image with ALMA CO (J=1-0 at $\lambda = 2.6 \text{ mm}$) contours from Sano et al. (2020) and the blue- and red-shifted optical ejecta. The eight new molecular clouds resolved by ALMA are likely interacting with shock waves and lie inside a wind-blown bubble. The X-ray emission from Cloud F shows enhanced abundances (e.g., Ne and O), indicating some clumps may be associated with the ejecta. Moreover, the CO ‘cloud F’ (Sano et al. 2020) in the ALMA image is somewhat offset from the optical and infrared neon

ejecta (see Figures 8b and 9), and lies between the blue- and red-shifted IR/optical ejecta. The angular resolutions of the ALMA image, $5''$, and the [Ne II] map, $4-6''$, are comparable. The peak of the dust emission in the $100 \mu\text{m}$ *Herschel* image (resolution $8''$) is located between CO ‘clouds E and F’. The central dust emission coincides with the neon infrared line emission from the ejecta and also with the optical ejecta (e.g., blue-shifted in blue contours). The peak of the dust emission lies between the ALMA CO ‘clouds E and F’. The angular separation between the central dust peak at $100 \mu\text{m}$ and the larger CO ‘cloud F’ is $23''$, which is 3 times larger than the *Herschel* beam size.

3.4. The Broad-band Spectral Energy Distribution of the Central Cold Dust

To derive dust masses associated with the central ejecta of N132D, we generated a spectral energy distribution (SED) from the MIR to submm for N132D in Figure 10. We chose the central ejecta only, since the *Herschel* images reveal clear detection from the central ejecta, whereas far-IR emission from NE ejecta are not distinct (see Figure 6). We combined *Spitzer* IRS spectra and *Herschel* photometry. The *Spitzer* spectra towards the center of the SNR only covered the $14-40 \mu\text{m}$ range and highlighted the broad dust features in the MIR.

We performed *Herschel* $100, 160, 250,$ and $350 \mu\text{m}$ photometry toward the central region because the emission there is clearly present at all wavelengths as shown in Figures 1f (marked as a circle) and 6. The exact area measured is an ellipse excluding a circular region covering CO ‘cloud F’ (Sano et al. 2020) and the shocked cloud (P12 in Dopita et al. 2018) as shown in Figure 9. Excluding this region minimizes the contribution from the ISM clouds, although the cloud’s contribution to far-IR is expected to be small. The shocked cloud ‘P7’ (Dopita et al. 2018) region has strong [O III] optical emission and highly blue-shifted O-rich knot emission, as shown in Figure 9c as well as infrared neon emission (green emission in Figure 9b). Note that the ‘P7’ region is small, and its flux is less than 5% of the total *Herschel* flux in the ellipse. Since N132D is known to be interacting with the surrounding ISM (the SNR shell emission is largely from shocked gas), we carefully selected the source and the background regions. For the latter, we averaged three elliptical regions, to the northwest, to the northeast and to the east. Their central coordinates are (R.A., Dec., a, b , PA) = $(81.2111^\circ, -69.6216^\circ, 32'', 27'', 357^\circ)$, $(81.3460^\circ, -69.6441^\circ, 25'', 25'', 357^\circ)$, and $(81.3627^\circ, -69.6169^\circ, 42'', 33'', 357^\circ)$. We avoided the region south of the SNR, since it is bright in far-IR from giant molecular clouds.

The $500 \mu\text{m}$ flux density is not included because the image does not resolve the central emission or the emission from N132D. It is not clear if the far IR emission at the position of the SNR is associated with the SNR or a part of a large ISM structure, probably due to the limited *Herschel* resolution ($36.4''$ at $500 \mu\text{m}$). The largest contribution to the flux uncertainty can originate from the background variation at the long IR wavelengths. We varied the choice of background region when measuring the flux density of N132D at various wavelengths, and found that it causes an increase of uncertainties from a few percent to a few tens of percent. The estimated flux

TABLE 1
SUMMARY OF INFRARED AND SUB-MILLIMETER OBSERVATIONS.

Date	Telescope	prog_id (PI)	Wavelengths (mode or resolution)
2004 November 7	<i>Spitzer</i> MIPS	3483 (Rho)	24 μm
2004 December 14	<i>Spitzer</i> IRS	3483 (Rho)	3 - 40 μm (staring)
2007 June 23	<i>Spitzer</i> IRS	30372 (Tappe)	5- 40 μm (staring), 14-40 μm (mapping)
2010 April 30	PACS+SPIRE	1342202224 (Meixner)	70(6''), 100(8''), 160(12''), 250(18''), 350(24.9'') & 500 μm (36.4'')
2010 May 4	<i>WISE</i>	survey	3.4(6''), 4.6(6''), 12(6''), 22 μm (6'')

TABLE 2
OBSERVED SPECTRAL LINE BRIGHTNESS

Wavelength (μm)	Line	Line Width (μm)	Surface Brightness (erg s ⁻¹ cm ⁻² sr ⁻¹)	de-reddened S.B. (erg s ⁻¹ cm ⁻² sr ⁻¹)
NE ejecta				
12.83 \pm 0.01	[Ne II]	0.127 \pm 0.003	6.90E-05 \pm 1.08E-06	6.95E-05 \pm 1.09E-06
15.57 \pm 0.01	[Ne III]	0.164 \pm 0.003	2.07E-05 \pm 3.89E-07	2.08E-05 \pm 3.91E-07
14.36 \pm 0.03	[Ne V]	0.414 \pm 0.067	3.74E-06 \pm 8.23E-07	3.76E-06 \pm 8.27E-07
24.32 \pm 0.02	[Ne V]	0.411 \pm 0.035	1.94E-06 \pm 1.67E-07	1.95E-06 \pm 1.67E-07
25.92 \pm 0.01	[O IV]	0.300 \pm 0.005	1.32E-05 \pm 1.96E-07	1.33E-05 \pm 1.97E-07
34.79 \pm 0.01	[Si II]	0.206 \pm 0.013	3.60E-06 \pm 2.28E-07	3.62E-06 \pm 2.29E-07
36.07 \pm 0.02	[Ne III]	0.171 \pm 0.023	6.97E-07 \pm 1.89E-07	6.99E-07 \pm 1.90E-07
Central Ejecta				
15.59 \pm 0.01	[Ne III]	0.188 \pm 0.003	1.15E-05 \pm 2.01E-07	1.16E-05 \pm 2.02E-07
25.95 \pm 0.01	[O IV]	0.384 \pm 0.005	8.40E-06 \pm 1.51E-07	8.40E-06 \pm 1.52E-07
34.89 \pm 0.01	[Si II]	0.253 \pm 0.014	2.82E-06 \pm 5.38E-07	2.85E-06 \pm 5.41E-07
Lasker's Bowl				
5.35 \pm 0.01	[Fe II]	0.059 \pm 0.002	2.90E-05 \pm 6.70E-07	2.92E-05 \pm 6.74E-07
6.99 \pm 0.01	[Ar II]	0.059 \pm 0.001	2.65E-05 \pm 3.75E-07	2.66E-05 \pm 3.76E-07
12.83 \pm 0.01	[Ne II]	0.121 \pm 0.002	4.23E-05 \pm 4.34E-07	4.26E-05 \pm 4.37E-07
14.40 \pm 0.01	[Cl II]	0.324 \pm 0.010	4.15E-06 \pm 1.37E-07	4.17E-06 \pm 1.38E-07
15.57 \pm 0.01	[Ne III]	0.157 \pm 0.001	1.89E-05 \pm 8.89E-08	1.90E-05 \pm 8.95E-08
17.94 \pm 0.01	[Fe II]	0.159 \pm 0.001	1.01E-05 \pm 5.90E-08	1.01E-05 \pm 5.95E-08
18.72 \pm 0.01	[S III]	0.147 \pm 0.004	3.68E-06 \pm 8.09E-08	3.71E-06 \pm 8.16E-08
24.50 \pm 0.07	[Fe II]	0.391 \pm 0.018	3.11E-06 \pm 1.48E-07	3.13E-06 \pm 1.49E-07
25.98 \pm 0.01	[Fe II]	0.297 \pm 0.003	1.24E-05 \pm 1.20E-07	1.24E-05 \pm 1.20E-07
33.45 \pm 0.01	[S III]	0.305 \pm 0.007	2.22E-06 \pm 5.50E-08	2.23E-06 \pm 5.52E-08
34.80 \pm 0.01	[Si II]	0.264 \pm 0.002	1.36E-05 \pm 9.77E-08	1.37E-05 \pm 9.80E-08
W complex				
5.36 \pm 0.01	[Fe II]	0.060 \pm 0.002	1.55E-05 \pm 5.13E-07	1.56E-05 \pm 5.16E-07
6.66 \pm 0.03	[Ni II]	0.067 \pm 0.007	3.20E-06 \pm 3.34E-07	3.22E-06 \pm 3.35E-07
7.02 \pm 0.01	[Ar II]	0.053 \pm 0.001	1.95E-05 \pm 2.64E-07	1.96E-05 \pm 2.65E-07
10.52 \pm 0.01	[S IV]	0.101 \pm 0.017	1.20E-06 \pm 2.60E-07	1.22E-06 \pm 2.65E-07
10.69 \pm 0.01	[Ni II]	0.168 \pm 0.027	2.24E-06 \pm 4.21E-07	2.28E-06 \pm 4.28E-07
12.85 \pm 0.01	[Ne II]	0.114 \pm 0.001	3.25E-05 \pm 2.19E-07	3.27E-05 \pm 2.21E-07
15.57 \pm 0.02	[Ne III]	0.155 \pm 0.003	1.52E-05 \pm 3.08E-07	1.53E-05 \pm 3.10E-07
17.95 \pm 0.01	[Fe II]	0.141 \pm 0.002	1.14E-05 \pm 1.04E-07	1.14E-05 \pm 1.05E-07
18.74 \pm 0.03	[S III]	0.162 \pm 0.006	3.37E-06 \pm 1.04E-07	3.40E-06 \pm 1.05E-07
24.57 \pm 0.05	[Fe II]	0.249 \pm 0.011	1.75E-06 \pm 7.63E-08	1.76E-06 \pm 7.67E-08
26.01 \pm 0.01	[Fe II]	0.288 \pm 0.003	8.13E-06 \pm 5.93E-08	8.17E-06 \pm 5.96E-08
33.56 \pm 0.02	[S III]	0.586 \pm 0.068	2.32E-06 \pm 2.69E-07	2.33E-06 \pm 2.70E-07
34.84 \pm 0.01	[Si II]	0.289 \pm 0.007	9.52E-06 \pm 2.25E-07	9.55E-06 \pm 2.26E-07

TABLE 3
COMPARISON OF THE LINE WIDTHS FROM DIFFERENT REGIONS

Region	Wavelength (μm)	FWHM (μm)	Velocity (km s ⁻¹)	Vel. shift. (km s ⁻¹)	Velocity _{true} (km s ⁻¹)
[Ne II]					
NE ejecta	12.827 \pm 0.001	0.127 \pm 0.003	2987 \pm 47	319 \pm 16	1513 \pm 91
Lasker's Bowl	12.828 \pm 0.001	0.121 \pm 0.002	2840 \pm 28	340 \pm 12	1197 \pm 65
West Complex	12.850 \pm 0.001	0.114 \pm 0.001	2676 \pm 16	806 \pm 7	726 \pm 57
[Ne III]					
NE ejecta	15.572 \pm 0.002	0.164 \pm 0.004	3167 \pm 60	410 \pm 22	1655 \pm 112
Center ejecta	15.595 \pm 0.002	0.187 \pm 0.003	3620 \pm 47	781 \pm 20	2411 \pm 70
Lasker's Bowl	15.572 \pm 0.001	0.157 \pm 0.001	3037 \pm 14	410 \pm 6	1390 \pm 31
West Complex	15.568 \pm 0.002	0.154 \pm 0.004	2982 \pm 60	307 \pm 25	1265 \pm 136

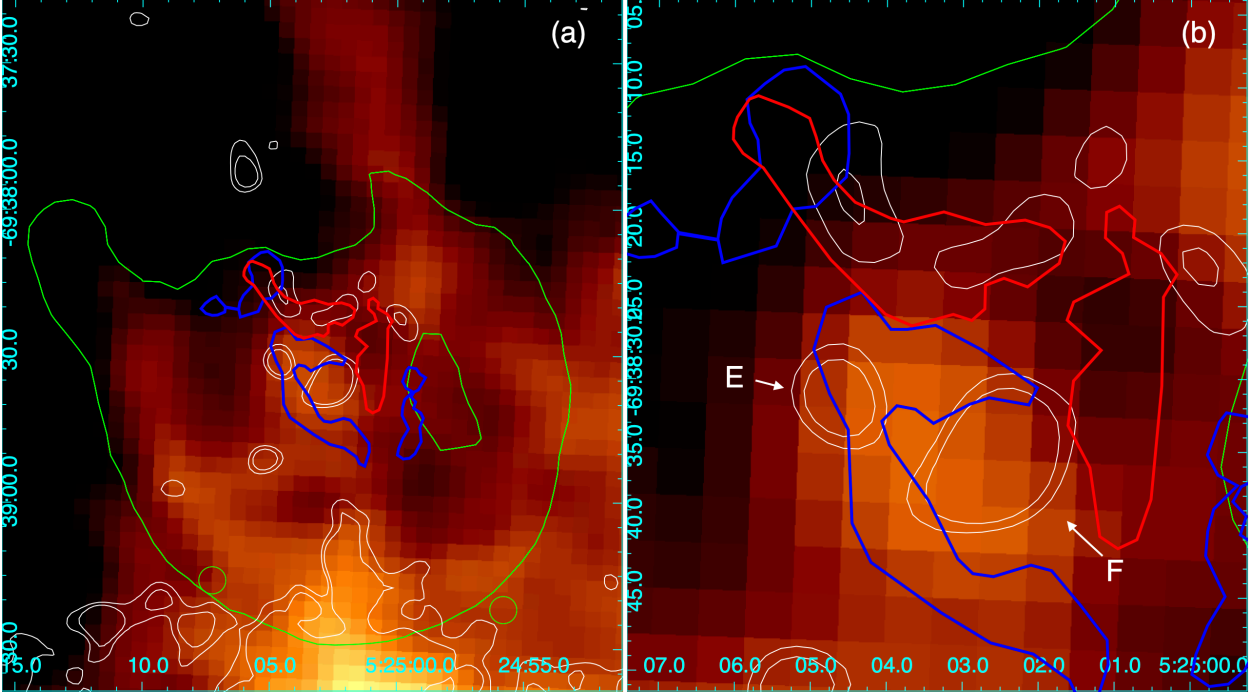


FIG. 8.— (a) The central blob of the *Herschel* 100 μm image of N132D coincides with the blue-shifted (blue contours) optical [O III] and is offset from the ALMA CO emission (white contours). The red-shifted optical [O III] emission is marked in red contours. The boundary of N132D 24 μm emission is marked as green contours. (b) Zoomed view of image (a) shows an offset between the *Herschel* dust blob and ALMA CO clumps labelled E and F.

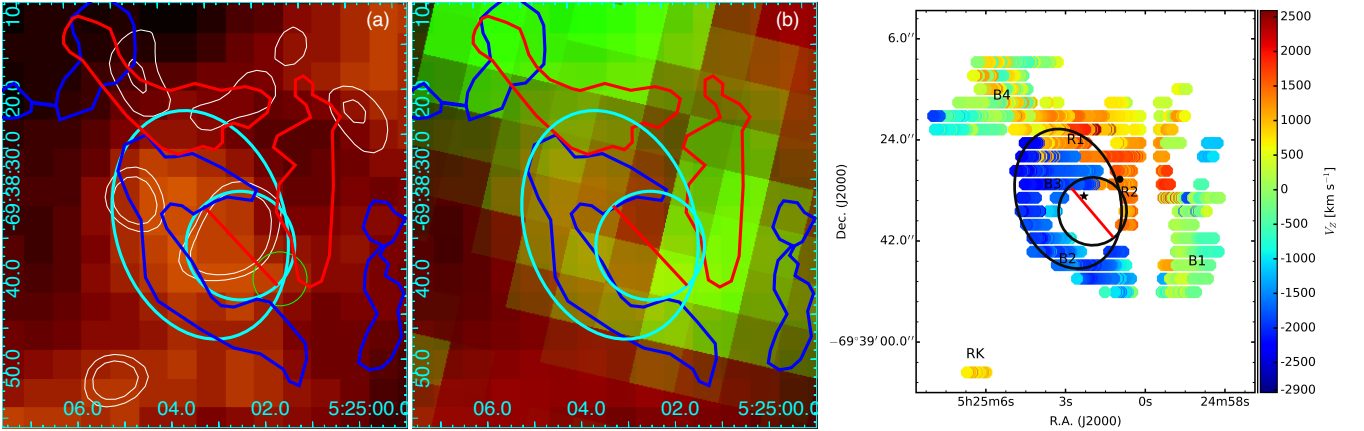


FIG. 9.— (a) The region used for *Herschel* photometry toward the central emission in constructing the SED (Fig. 10) is marked as an ellipse (in cyan), but excludes a circular region (in cyan with a red diagonal solid line) toward the central blob on the *Herschel* 100 μm image. The exact region is an ellipse of (R.A., Dec., a , b , PA) = (81.2635°, -69.6429°, 9'', 13'', 17°) where a is a major axis, b is a minor axis, and P.A. is a position angle from the north; the excluded circular region is centered on (R.A., Dec.) = (81.260° -69.643°) and has a radius of 6''. Excluded regions include the CO ‘cloud F’ on the ALMA image (see Fig. 8) and shocked cloud, P12 (marked as a green circle from Dopita et al. (2018)). (b) Infrared [Ne III] image in green is added to the image (a) without the CO contours. (c) The same regions (in black) are marked on a high-velocity optical ejecta image (adapted from Fig. 5 of Law et al. 2020) with color-coded velocity information.

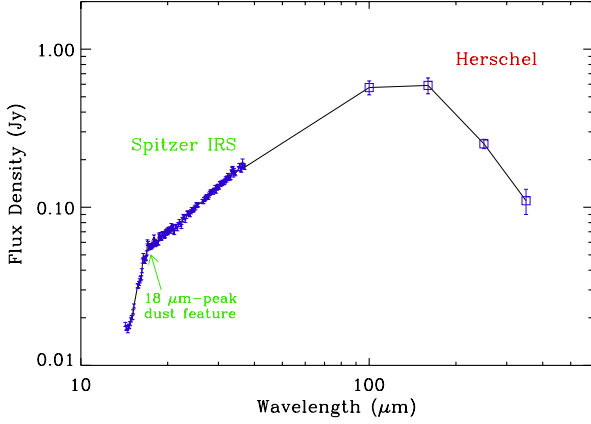


FIG. 10.— Spectral energy distribution of N132D towards the central ejecta emission. The data (in blue) include *Spitzer* IRS and *Herschel* photometry. The 18 μm -peak dust feature is marked. The detection of the emission at 500 μm is uncertain; see text for details.

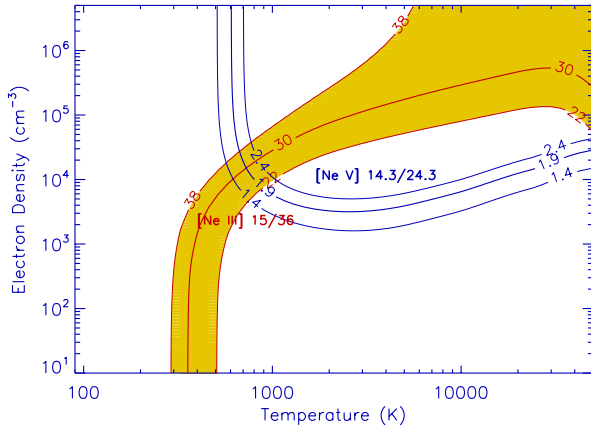


FIG. 11.— Line diagnostic contours of the ratios of [Ne III] 15/36 μm (red) and [Ne V] 14.3/24.3 μm (blue) at location of the NE ejecta. The observed ratios are denoted by thick solid lines imply most likely values of [Ne III] = 30 and [Ne V] = 1.92. Note that the density is an electron density. The shaded region (in yellow) shows the range of temperatures and densities allowed by errors for the [Ne III] ratio, whereas the allowed physical conditions of [Ne V] lines are marked with the thick blue contour lines.

densities of N132D in far-IR and submm are summarized in Table 5.

4. DISCUSSION

4.1. Neon Ejecta and Line-Flux Ratio

In the line list in Table 2, the ions [Ne III] and [Ne V] are suitable diagnostics for constraining densities and temperatures of the ionized gas.

The measured line flux ratios for [Ne V] 14.3/24.3 μm are 1.92 ± 0.45 , and 29.8 ± 12 for [Ne III] 15.6/36 μm . The [Ne V] ratio in N132D is similar to, but slightly higher than that in 1E0102 (1.76 ± 0.11 Rho et al. 2009) while the [Ne III] ratio in N132D is almost a factor of 2 smaller than that in E0102 (54 ± 28). The ratio $I_{15.6}/I_{36}$ μm is assigned an additional 50% systematic error for the 36 μm line intensity, because this line falls on the degrading part of the array. To constrain temperatures and densities, we calculated the line intensities and ratios of [Ne V] and [Ne III]. We solved the excitation-rate equations, including collisional and radiative processes, as a matrix

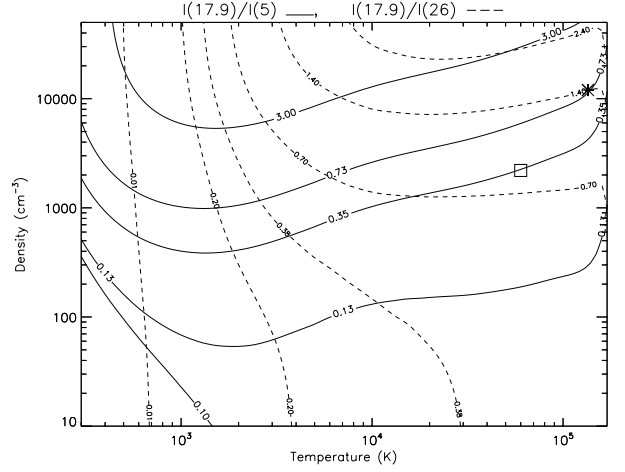


FIG. 12.— Contour plots of [Fe II] diagnostic line ratios using 5.3, 17.9, and 26 μm lines. Lasker's Bowl has a temperature of 6×10^4 K and a density of 2200 cm^{-3} (marked as a square) and the West Complex has a temperature of 1.3×10^5 K and a density of $12,000 \text{ cm}^{-3}$ (marked as an asterisk).

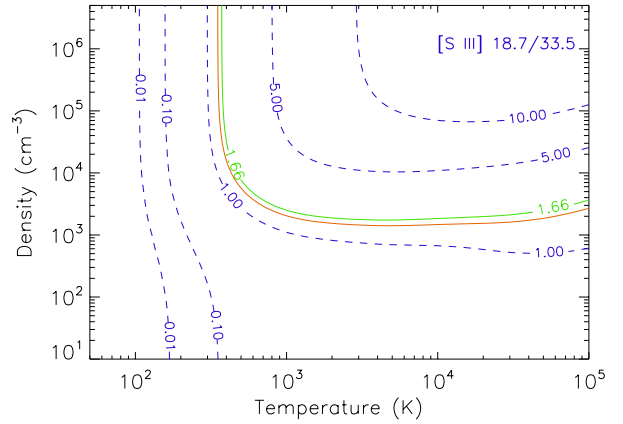


FIG. 13.— Line diagnostic contours of the ratios of [S III] 18.7/33.5 μm . The contours for the Lasker's Bowl (with the ratio of 1.66) and West Complex (1.46) are marked in green and brown, respectively.

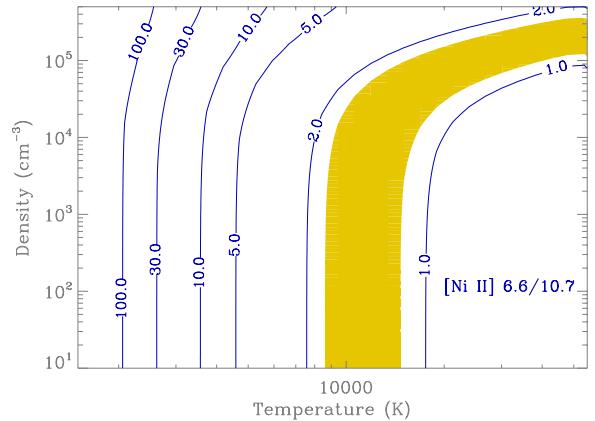


FIG. 14.— Line diagnostic contours of the ratios of [Ni II] 6.6/10.7 μm . The shaded region (in yellow) shows the range of temperatures and densities allowed by errors for the [Ni II] ratio. The [Ni II] ratio is a temperature indicator and implies $T > 8000$ K.

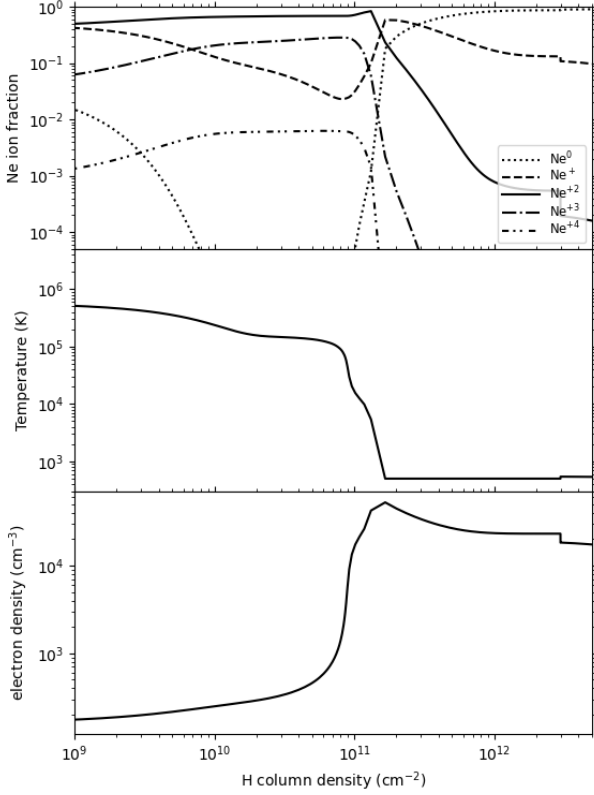


FIG. 15.— Neon ionization (above) and gas temperature (below) in the shock for our model with shock speed 90 km s^{-1} and ram pressure $20\times$ the Blair et al. (2000) assumed value. The ionization of Ne clearly shows the lag in ionization and recombination in the ionization ($T \geq 10^5 \text{ K}$) and cooling ($10^3 < T \leq 10^5 \text{ K}$) zones. The region on the right, where $T \sim 540 \text{ K}$, is photoionized and assumed to be in thermal and ionization equilibrium. The Ne^{+4} ion fraction is very low in the photoionized zone and so the observed $[\text{Ne V}]$ $14.3 \mu\text{m}$ and $24.3 \mu\text{m}$ emission come from the cooling zone (with electron density $10^3 - 5 \times 10^4 \text{ cm}^{-3}$) whereas most of the $[\text{Ne II}]$ and $[\text{Ne III}]$ emission comes from the photoionized zone.

using 5 energy levels for $[\text{Ne V}]$ and 3 levels for $[\text{Ne III}]$. The atomic data are described in Rho et al. (2009). The contours of their ratios are marked in Figure 11 and Table 4 lists the inferred density and temperature ranges.

Radiative shock models for a range of shock velocities, including the effects of photoionization, were produced by Rho et al. (2009) to understand the $[\text{Ne III}]$ and $[\text{Ne V}]$ lines of E0102. The shock models indicate that the $[\text{Ne V}]$ lines come mainly from the cooling zone, in which the temperature is falling sharply from hot to cold, whereas $[\text{Ne III}]$ comes mainly from the photoionization zone, which has a low temperature. We present and discuss the shock models and derive the physical conditions of Ne ejecta of N132D in Section 4.3.

4.2. Line diagnostics of $[\text{Fe II}]$, $[\text{S III}]$, and $[\text{Ni II}]$ lines in dense knots

4.2.1. CSM and ISM dense knots

Lasker’s Bowl and the West Complex (see Figure 1) are known to be luminous and to contain dense shocked clouds (dense knots, hereafter) with interstellar composition and a $\sim 200 \text{ km s}^{-1}$ velocity dispersion in optical lines (Blair et al. 2000). The dense knots are suggested to be either ISM or mass loss material (CSM) from the

progenitor (Blair et al. 2000; Sutherland & Dopita 1995). The optical spectroscopy of the West Complex indicates that collisional de-excitation of 6716\AA is largely responsible for the relatively low $[\text{S II}]$ $6724\text{\AA}/\text{H}\alpha$ ratio observed as compared with many SNRs. The optical $[\text{S II}]$ emission arises in the compressed postshock medium behind the shock and implies a preshock cloud density of greater than 100 cm^{-3} (Blair et al. 2000). Shock velocities of order $\sim 200 \text{ km s}^{-1}$ are needed to generate the emission from high-ionization species such as the UV lines of O IV , N V , and $[\text{Ne IV}]$. Such shocks produce sufficient high-energy photons in the postshock region to ionize the upstream gas before it enters the shock (Shull & McKee 1979; Hartigan et al. 1987; Sutherland et al. 1993). Blair et al. (2000) assumed complete preionization of H and 85% preionization of He to He^+ . Most H α emission (with $\sim 200 \text{ km s}^{-1}$) arises in the recombination zone of the cloud shocks, which have velocities similar to nearby H II regions (Dopita et al. 2018).

The IRS spectra of Lasker’s Bowl and the West Complex reveal that these regions emit strongly in $[\text{Fe II}]$, $[\text{Ar II}]$, $[\text{S III}]$, and $[\text{Ni II}]$ lines as shown in Figure 4. In Lasker’s Bowl the $[\text{Fe II}]$ ratio between $17.9 \mu\text{m}$ and $5 \mu\text{m}$ lines ($[\text{Fe II}]$ $I_{17.9}/I_5$) is 0.35 ± 0.01 and the $[\text{Fe II}]$ ratio between $17.9 \mu\text{m}$ and $26 \mu\text{m}$ ($[\text{Fe II}]$ $I_{17.9}/I_{26}$) is 0.81 ± 0.01 .

4.2.2. Line diagnostics of $[\text{Fe II}]$, $[\text{S III}]$, and $[\text{Ni II}]$ lines

Diagnostics of the $[\text{Fe II}]$ lines use excitation rate equations presented in (Hewitt et al. 2009; Rho et al. 2001). Figure 12 shows contours of line ratios $17.9/5.35 \mu\text{m}$ and $17.9/26 \mu\text{m}$ as functions of density and temperature; the former ratio is sensitive mainly to density, and the latter ratio is dependent on both density and temperature. We used temperature-dependent atomic data from Ramsbottom et al. (2007) and 46 levels of $[\text{Fe II}]$ lines. The derived densities and temperatures for each of the Lasker’s Bowl and West Complex positions are summarized in Table 4. The densities ($2000 - 12000 \text{ cm}^{-3}$) of both of these regions of CSM/ISM knots are higher than those ($< 1000 \text{ cm}^{-3}$) in SNRs interacting with molecular clouds (Hewitt et al. 2009) and the temperatures ($6 - 13 \times 10^4 \text{ K}$) are also higher.

In the same manner, we construct line diagnostic plots for $[\text{S III}]$ $I_{18.7}/I_{33.48}$ and $[\text{Ni II}]$ $I_{18.7}/I_{33.48}$. The estimated ratios are listed in Table 4. For $[\text{S III}]$ lines, we solve 4-level system excitation rate equations and use the temperature-dependent atomic data from Galavís et al. (1995) and Galavís et al. (1998). Figure 13 shows $[\text{S III}]$ line diagnostics the measured ratio implies a density $> 10^3 \text{ cm}^{-3}$. For a gas temperature $> 600 \text{ K}$, the density is $10^3 - 3 \times 10^3 \text{ cm}^{-3}$, and for gas with a temperature of $300 - 400 \text{ K}$, the density is $> 10^4 \text{ cm}^{-3}$. For the $[\text{Ni II}]$ lines, we solve 8-level system excitation rate equations and use the temperature dependent effective collision strengths from Bautista (2004). The $[\text{Ni II}]$ lines are potentially good temperature indicators. Figure 14 shows $[\text{Ni II}]$ line diagnostics; the observed ratio $I_{18.7}/I_{33.48}$ indicates a gas temperature $> 8000 \text{ K}$. The inferred densities and temperatures from various line ratios are summarized in Table 4.

TABLE 4
PHYSICAL PROPERTIES FROM SAME-ION LINE FLUX RATIOS IN DENSE KNOTS

Region	Line	Wavelengths	Ratio	T (K) ^a	n _e (cm ⁻³) ^a
Ejecta	[Ne V]	24.3/14.3 μm	1.92±0.45	500 - 10 ⁵ K	>10 ³ (e.g., 10 ³ - 10 ⁴)
			shock model ^b	10³ - 10⁴ K	10³ - 5×10⁴
	[Ne III]	15.6/36 μm	29.8±12	300 - 5×10 ⁴ K	100 - 5×10 ⁶
Lasker's Bowl (CSM/ISM knots)	[Fe II]	17.9/5 μm	0.35±0.01		
			0.82±0.01	6×10⁴ K	2200
	[S III]	18.71/33.48 μm	1.66±0.06	> 600 K or 300-400 K	10³ - 3×10³ >10 ⁴
West Complex (ISM/CSM knots)	[Fe II]	17.9/5 μm	0.73±0.03		
			1.40±0.02	1.3×10⁵ K	1.2×10⁴
	[S III]	18.71/33.48 μm	1.46±0.18	> 600 or 300-400 K	10³ - 3×10³ >10 ⁴
	[Ni II]	6.63/10.7 μm	1.4±0.3	> 8000 K	any

^aThe best values are marked in bold characters. ^bSee Section 4.3 for details.

TABLE 5
FIR-SUBMM FLUX DENSITIES.

Data	Wavelength (μm)	Flux Density (Jy)
<i>WISE</i> (w3)	12	0.015±0.010
<i>Spitzer</i> MIPS	24	0.090±0.006
<i>Herschel</i> PACS	100	0.572±0.058
<i>Herschel</i> PACS	160	0.590±0.068
<i>Herschel</i> SPIRE	250	0.252±0.017
<i>Herschel</i> SPIRE	350	0.110±0.020

4.3. Application of shock models and physical conditions in ejecta

We carried out calculations of the shock profiles similarly to the way we did for 1E0102 (Rho et al. 2009) but using the lower ram pressure and shock speeds from Blair et al. (2000) for N132D. We have now also developed the capability to simulate shocks with only partial electron-ion temperature equilibration at the front, i.e. following the electron and ion temperatures separately including their evolution toward equilibration. We made the calculations assuming an initial 50% equilibration. As in Rho et al. (2009) we combine the steady shock calculation of the hot post-shock region and cooling region with a calculation of the cooled photoionized zone that uses Cloudy (Ferland et al. 2017). The shocks produce hot gas just behind the front which ionizes the pre-shock gas. Further behind the shock, cooling leads to a sharp drop in temperature in the recombination zone, where the gas is overionized. Once the gas has cooled to low temperatures, it is maintained by the ionizing radiation from the upstream regions that heats the gas and balances cooling in the photoionized region. The steady-state shock calculation uses ionizing radiation only from the forward shock and calculates the non-equilibrium ionization. The photoionized region calculation includes emission generated in the forward shock as well as that is generated in the reverse shock, but assumes equilibrium ionization.

We find that matching the emission ratio [Ne III] 15.6 μm/[Ne II] 12.8 μm as well as matching the flux of [Ne II] 12.8 μm emission requires shocks with speeds

of $\sim 90 - 150 \text{ km s}^{-1}$. In order to match the optical HST data for the N132D ejecta, Blair et al. (2000) explored models with a range of shock velocities with a constant ram pressure of $nv_{sh}^2 = 100 \text{ cm}^{-3} \text{ km}^2 \text{ s}^{-2}$, and magnetic field given by $B/n^{1/2} = 0.1$ (where the magnetic field, B , is in μG and density, n , is in cm^{-3}). We found that higher pressures and magnetic fields were needed than used by Blair et al. (2000), and explored combinations of factors of 10 to 20 times the values for the ram pressure and magnetic field. We found acceptable solutions for several different shock velocities, although solutions that also matched the [Ne V] 14.3 μm/24.3 μm ratio required high ram pressures, $\sim 20\times$ the Blair et al. (2000) value. The model that best matches our data has a pre-shock density n of $\sim 25 \text{ cm}^{-3}$ and shock velocity v_{sh} of $\sim 100 \text{ km s}^{-1}$. We assumed the same abundances as Blair et al. (2000) (logarithmic relative to H with H = 12.00) O = 16.00, Ne = 15.25, C = 14.50, and Mg = 13.50. Figure 15 illustrates the Ne ionization and temperature for the two parts of the calculation for one model. In the post-shock photoionized region, these models lead to values of $\sim 1000 - 2 \times 10^4 \text{ cm}^{-3}$ for the electron density and temperatures of $\sim 300 - 600 \text{ K}$. Essentially all of the [Ne II] emission comes from the photoionized zone in these models, while [Ne III] emission comes from both the recombination zone and the photoionized zone. In the post-shock cooling region, the [Ne V] emission peaks near the location where the electron density peaks and the temperature and ion fraction of Ne^{+4} have begun to drop. None of the [Ne V] emission comes from the photoionized zone.

4.4. Synchrotron contribution to the dust emission

We estimated the contribution of synchrotron emission to the infrared spectrum using the radio fluxes and spectral index. The radio flux is 1.5 Jy at 6 cm for the entire SNR (Dickel & Milne 1995). We estimated the contribution of the flux to the emission from the central ejecta region using the 5 GHz radio image, and found that it is 12% of the flux from the entire SNR. For a radio spectral index $\alpha = -0.70$ (Dickel & Milne 1995), where $S_\nu \propto \nu^\alpha$, this is a very small contribution to the infrared continuum ($< 1\%$, see the dotted line in Figures 16 and 17).

4.5. Dust model fitting

To estimate the dust mass, spectral fitting was performed using a chi-squared-minimizing routine (*mpfit* routine by Markwardt 2009) which was applied to the SED of N132D. The detailed method is described in Rho et al. (2018). The flux $F_\nu^i = \sum_i C_i B_\nu 3 Q_{abs,i} / (4 a \rho_i)$, where the $Q(\lambda, a)$ are calculated using Mie theory (Bohren & Huffman 1985) and the continuous distributions of ellipsoidal (CDE) model for silicate dust, a is the dust particle size, ρ_i is the bulk density, and B_ν is the Planck function for each of grain species (i). We derived the scale factor C_i and estimated dust masses which are summarized in Table 6.

We calculated Q_{abs} from n and k values of Al_2O_3 (Begemann et al. 1997), but the values only cover up to $500 \mu\text{m}$. Therefore, we extended the power law of the Q_{abs} between 450 and $500 \mu\text{m}$ to $1000 \mu\text{m}$, although it doesn't affect the quality of the fit since the observed data only cover up to $350 \mu\text{m}$. The same absorption coefficients from various grains were applied to G54.1+0.3 and Cas A (Rho et al. 2018).

We first performed spectral fitting of the $18 \mu\text{m}$ -feature using carbon, enstatite (MgSiO_3) and forsterite (Mg_2SiO_4). Note that the synchrotron component is fixed as described in Section 4.4 (see the dotted green lines in Figures 16 and 17). The feature is reasonably reproduced by Mg_2SiO_4 alone (Model A4 in Table 6 and Figure 16), a combination of MgSiO_3 and Mg_2SiO_4 (Models A2 and A4), or MgSiO_3 and Al_2O_3 (Model A5). Pure carbon dust fails to reproduce the $18 \mu\text{m}$ feature. The result of the fitting is a smaller χ^2 (Model A1 of Table 6) than those of other models. Table 6 summarizes the dust spectral fitting results and dust masses (Models A1 to A6). The values of the reduced χ^2 are small (~ 0.5) and they are similar to each other (Models A2-A6) except for Model A1, which is a much poorer fit. Model A1 is excluded because significant residuals appear around $100 \mu\text{m}$ and the $18 \mu\text{m}$ dust feature, which lead to a high reduced χ^2 .

The cold component dominates the dust mass; the yielded dust mass is $1.60 M_\odot$ for silicate dust of MgSiO_3 and Mg_2SiO_4 (Model A5), $0.79 M_\odot$ for Carbon (Models A2 and A3), and $0.17 M_\odot$ for the cold component of Al_2O_3 (Model A5 in Table 6). We attempted a dust fitting with two cold dust components, MgSiO_3 and carbon, where we set their temperatures to $\geq 20 \text{ K}$ (because the infrared cirrus has a temperature below 20 K ; Reach et al. (1995); Reach & Rho (2000)). Doing this results in significant dust masses from both types of dust (see Model A6 in Table 6). The simple dust model by Dwek et al. (2007) predicts that 84% of the dust is silicate, 10% is carbon, and 6% is other types for a $40 M_\odot$ progenitor star. The dust mass from Model A6 is $1.25 \pm 0.28 M_\odot$, which is between the dust masses assuming silicate ($1.6 \pm 0.3 M_\odot$) and carbon dust ($0.79 \pm 0.19 M_\odot$).

The theoretical models of dust formation predict more than ten different grain species are formed in SN ejecta (Sluder et al. 2018; Marassi et al. 2019; Sarangi & Cherchneff 2015). Dust formation in SN Ib has been modeled by Nozawa et al. (2008), who predicted FeS and Fe_3O_4 grains as well as the grains included in our fits. We did not experiment with using these two grain types since they produce strong dust features around $30 - 40$

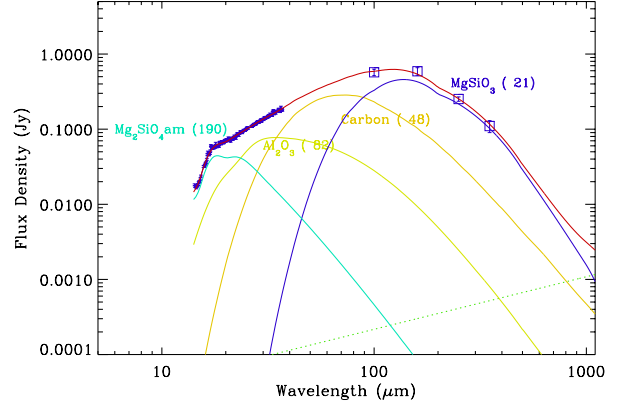


FIG. 16.— Model A4 (Table 6) is superposed on *Spitzer* IRS spectra and *Herschel* photometry of N132D. The grains of Mg_2SiO_4 and MgSiO_3 reproduce the $18 \mu\text{m}$ feature and cold dust, respectively. The number in parenthesis is dust temperature for each type of grain. Synchrotron radiation (green dotted line) is included in the fitting, but makes only a minor contribution.

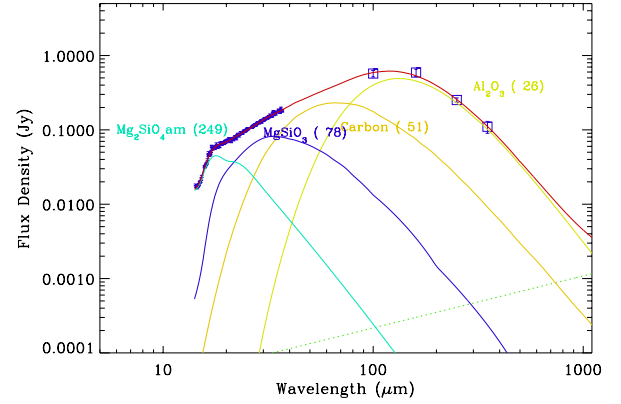


FIG. 17.— Model A5: *Spitzer* IRS spectra and *Herschel* photometry of N132D with one (Model A5 in Table 6) of the best-fitting dust models superposed. The dust compositions include Carbon/ Mg_2SiO_4 and carbon dust to fit the $18 \mu\text{m}$ feature. The dust compositions include MgSiO_3 , Mg_2SiO_4 , Carbon dust and Al_2O_3 . Synchrotron radiation (green dotted line) is included in the fitting, but makes only a minor contribution.

μm , which are not observed in N132D. We also use Mg_2SiO_4 dust as a cold component, but the χ^2 minimization strongly favors other dust composition such as MgSiO_3 , carbon or Al_2O_3 as listed in Table 6. We conclude the dust mass is $1.25 \pm 0.65 M_\odot$ where $1.25 M_\odot$ is from Model A6; the uncertainties are a combination of the lower limit of carbon dust (Model A3) and the upper limit of silicate (MgSiO_3) dust (Model A4) models.

We attempted to apply the three-component (unshocked, clumped, and diffuse) physical models of dust emission (called “DINAMO”) of Priestley et al. (2019, 2022) to the N132D data. The model has been exclusively applied to the SNR Cas A (Priestley et al. 2019, 2022). We calculated dust SEDs using the DINAMO model (Priestley et al. 2019) for a single grain size in each component, then fit the N132D data with the dust mass in each component as our three free parameters. Fitting was done using the Monte Carlo Markov chain code ‘emcee’ (Foreman-Mackey et al. 2013). However, we conclude that for N132D, the four far-IR data points from 100 to $250 \mu\text{m}$ and the limited input parameters pertaining to its cold gas) were not adequate to disen-

TABLE 6
DUST SPECTRAL FITTING RESULTS AND ESTIMATED DUST MASS.

Model	$\Delta\chi^2(=\chi^2/\text{dof})$	18 μm feature dust (K, M_\odot)	other compositions (T, M_d) (K, M_\odot)	cold (T, M_d) dust (K, M_\odot)	total (M_d) (M_\odot)
A1	3.34	Carbon (107, 3.7E-4)	Mg ₂ SiO ₄ (54, 5.1E-8), MgSiO ₃ (38, 0.084)	Al ₂ O ₃ (25, 0.235)	1.84
A2	0.53	MgSiO ₃ (700, 1.0E-7) ($>300, \pm 0.2\text{E-}7$)	Mg ₂ SiO ₄ (85, 3.6E-4), Al ₂ O ₃ (40, 0.008) ($\pm 3, \pm 0.9\text{E-}4$), ($\pm 2, \pm 0.002$)	Carbon (24, 0.77) ($\pm 2, \pm 0.15$)	0.78 ± 0.15
A3	0.40	Mg ₂ SiO ₄ (245, 1.78E-6) ($\pm 14, 0.40\text{E-}6$)	MgSiO ₃ (75, 6.80E-4), Al ₂ O ₃ (44, 0.013) ($\pm 3, \pm 2.3\text{E-}4$), ($\pm 4, \pm 0.007$)	Carbon (23, 0.779) ($\pm 3, \pm 0.181$)	0.79 ± 0.19
A4	0.45	Mg ₂ SiO ₄ (190, 4.5E-5) ($\pm 10, 1.3\text{E-}5$)	Al ₂ O ₃ (83, 3.7E-4), Carbon (48, 0.03) ($\pm 7, \pm 5.8\text{E-}4$), ($\pm 8, \pm 0.03$)	MgSiO ₃ (21, 1.565) ($\pm 2, \pm 0.03$)	1.60 ± 0.30
A5	0.40	Mg ₂ SiO ₄ (249, 1.6E-5) ($\pm 5, \pm 0.5\text{E-}6$)	MgSiO ₃ (78, 4.4E-4), Carbon (51, 0.020) ($\pm 6, \pm 3.3\text{E-}4$), ($\pm 6, 0.014$)	Al ₂ O ₃ (26, 0.150) ($\pm 2, \pm 0.03$)	0.17 ± 0.04
A6^a	0.52	Mg₂SiO₄ (182, 6.8E-6) ($\pm 2, \pm 0.4\text{E-}6$)	Al₂O₃ (61, 1.4E-4) ($\pm 1, \pm 1.4\text{E-}4$)	MgSiO₃ (25 ^b , 0.863 \pm 0.150) + C (20 ^b , 0.386 \pm 0.234)	1.25\pm0.28

^aThe best values are marked in bold characters. ^bThe temperatures were set to be ≥ 20 K since the dust below 20 K belongs to cold ISM.

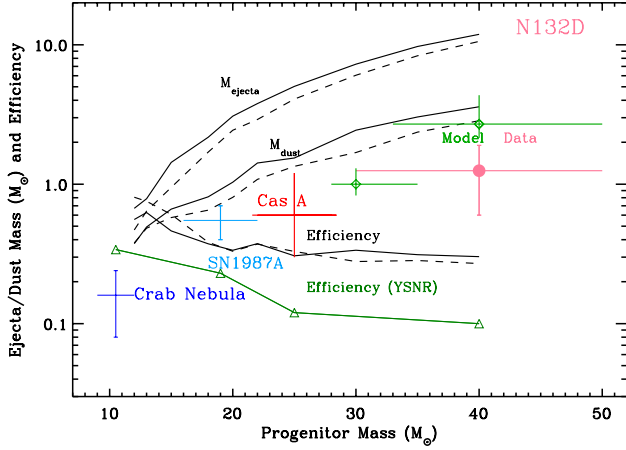


FIG. 18.— Ejecta mass (M_{ejecta}), dust mass (M_{dust}), and dust formation efficiency ($\text{Efficiency} = M_{\text{dust}}/M_{\text{ejecta}}$) curves as a function of progenitor mass (Dwek et al. 2007) with the dust mass of N132D. The dashed curves are for low metallicity. The observed dust mass of N132D (a filled circle in pink) is the results from the spectral fits in Table 6. The upper and lower diamonds (green) are predicted dust masses from two different models (CE-0 and CE-2 with $[\text{Fe}/\text{H}]=0$ and $[\text{Fe}/\text{H}]=-2$, respectively) for 30–40 M_\odot progenitor stars (Marassi et al. 2019). The errors were estimated by interpolation between the model grids. The dust masses of other YSNRs, namely Cas A, SN1987A, and the Crab Nebula, are also shown (Table 7). The dust condensation efficiency is marked as “Efficiency (YSNR)” derived from the ratio of observed dust mass to total ejecta mass (M_{ejecta}). Both models and observations suggest that the dust mass in N132D is likely higher than the other three SNRs, but the uncertainty is large and depends on the dust composition.

tangle the physical processes of heating and cooling that occur in the three phases.

4.6. Progenitor mass of N132D

Ground-based optical studies by Sutherland & Dopita (1995) and Morse et al. (1995) show that the O-rich ejecta filaments extend to a radius of 6 pc from the remnant center. HST WFPC2 images distinguish the ejecta from shocked circumstellar clouds (Morse et al. 1996). Blair et al. (2000) suggested that the progenitor mass of N132D is between 30 and 35 M_\odot . The HST spectrographic observations found a silicon-to-oxygen abundance ratio (~ 0.01) which is consistent with the model

of a progenitor of 50 M_\odot (France et al. 2009). Therefore, we use a progenitor mass of N132D of 40 ± 10 M_\odot (see Figure 18). Recent observations of SN 2019hgp show a rich set of carbon, oxygen, and neon emission lines, which suggest a massive progenitor star (Gal-Yam et al. 2021). SN 2019hgp may be similar to the early stage of N132D.

Recently Sharda et al. (2020) carried out X-ray observations of N132D and detected Fe lines. They infer a low Fe abundance and a progenitor mass of 15 M_\odot . However, we detected many Fe lines from the CSM/ISM knots (such as Lasker’s Bowl or West Complex in Table 4; see Blair et al. (2000)). These are not high-velocity ejecta knots. Thus we believe that contamination from CSM/ISM knots could have caused Sharda et al. (2020) to infer the lower progenitor mass. Siegel et al. (2021) suggest caution about using the X-ray Fe line as the sole diagnostic for typing a remnant.

4.7. Dust in N132D and in the early Universe

4.7.1. Dust mass as a function of progenitor mass

We show predicted ejecta and dust masses as a function of progenitor mass and the observed dust masses of N132D in Figure 18. The amount of dust as a function of progenitor mass is given by Dwek et al. (2007). Their calculation is based on the nucleosynthesis model and ejecta mass described in Woosley & Weaver (1995). The dust masses of other YSNRs of the Crab Nebula, SN 1987A, and Cas A (see Table 7) are also marked.

Dwek et al. (2007) modeled the mass of silicate dust, carbon dust, and other compositions (Ca-Ti-Al), and the total dust mass as a function of progenitor with the assumption of no dust destruction (see Figure 18). For a 35 M_\odot progenitor, the total dust yield is 3.04 M_\odot , where silicate, carbon, and Ca-Ti-Al type dust are 2.56 (84% of the total), 0.32 (10%), 0.16 (6%) M_\odot , respectively. In contrast, Morgan & Edmunds (2003) predict the yield of carbon dust is similar to that of silicate dust. Nozawa et al. (2008) calculated a total dust mass of 1.5 M_\odot for a type Ib SN model of which carbon dust is about half, 0.7 M_\odot . We obtain a dust mass of 0.6–1.9 M_\odot for N132D. This is a factor of 1.3–2 times higher than those of the other four YSNRs (see Figure 18), whose progenitor masses are each lower than N132D. The estimated dust mass for N132D is comparable to some theoretical

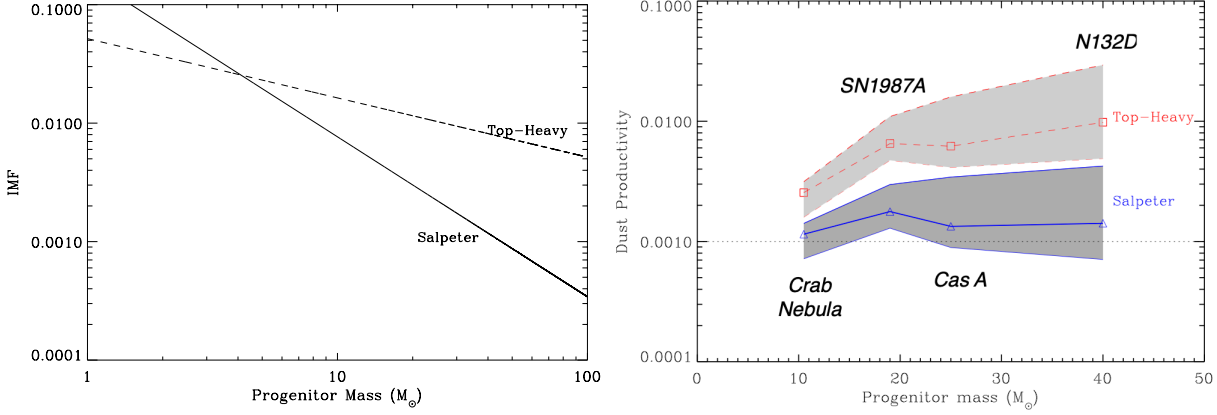


FIG. 19.— The Salpeter and top-heavy IMFs (left: *a*) and dust productivity (right: *b*) are shown in solid and dashed lines, based on the definitions in Gall et al. (2011), and Dwek & Cherchneff (2011). The dust productivities are estimated based on the observed dust masses from the YSNRs, Crab Nebula, SN1987A, Cas A, and N132D (thick lines) with squares symbols (Salpeter IMF) and triangles (top-heavy IMF) with errors (grey). The upper limits are from theoretical dust yields (Dwek et al. 2007), which assume no dust destruction, and the lower limits are from observations. The dotted line is the critical dust productivity ($\mu_D(\text{crit})$, see the text for details).

TABLE 7
SUMMARY OF DUST MASS FROM *Herschel* - DETECTED YOUNG SUPERNOVA REMNANTS.

SNR	dist (kpc)	diameter (')	radius (pc)	age (yr)	dust mass (M_\odot)	dominant dust type	progenitor (M_\odot)	ref.
SN1987A	51	0.02	0.2	35	0.4-0.7	carbon	18-20: Type II	1
Cas A (G111.72.1)	3.4	5	2	350	0.3-0.5	silicate	25-30: Type II/Ib	2, 3
Crab Nebula (G184.65.8)	2	7	1.7	968	0.1-0.54	carbon	10-12: Type IIP	4, 5, 6
G54.1+0.3	5	1.5	1	2900	0.08-0.9	silicate	15-35 (25 \pm 10): Type II?	6, 7
G21.5-0.9	4.6	5	3	<1000	0.29 \pm 0.08	...	10	8, 9
N132D	51	1.6	12.5	2500	1.25 \pm 0.65	...	30-50: Ib c	10, this paper

^a References are: (1) Matsuura et al. (2015); (2) De Looze et al. (2017); (3) Rho et al. (2008); (4) Gomez et al. (2012); (5) Owen & Barlow (2015); (6) Temim et al. (2012); (7) Rho et al. (2018); (8) Guest et al. (2019); (9) Chawner et al. (2019); (10) Law et al. (2020)

dust masses (Marassi et al. 2019). A dust mass of $\sim 1 M_\odot$ per ccSN is needed to explain the dust observed in the early Universe (Dwek et al. 2007). N132D is likely an example with a higher than average dust mass for a young SN.

The progenitor and dust masses of Cas A, SN1987A, the Crab Nebula, G54.1+0.3, and G21.5-0.9, together with N132D are listed in Table 7. 1E0102 (1E 0102-7219 or SNR B0102-72.3) (Rho et al. 2009) is not included since its *Herschel* observation was not usable due to a bright H II region near 1E0102 and *Herschel*'s limited spatial resolution. Thus the dust mass of 1E0102 only using *Spitzer* data could not be compared with that of N132D. The progenitor and dust masses of G54.1+0.3 and G21.5-0.9 are similar to those of Cas A and the Crab Nebula,. The dust mass of N132D is up to a factor of two higher than those of Cas A, SN1987A, G54.1+0.3, and the Crab Nebula (De Looze et al. 2017; Matsuura et al. 2011; Indebetouw et al. 2014; Matsuura et al. 2015; Rho et al. 2018; Gomez et al. 2012; Owen & Barlow 2015) as shown in Figure 18. The higher dust mass of N132D is consistent with the fact that its progenitor mass (30 - 50 M_\odot) is higher than those of the other YSNRs.

Dust formation models for higher mass progenitors are limited in number. Marassi et al. (2019) include models of SN Type Ib and show that dust masses of 1.4 - 3.4 M_\odot (marked as diamonds in Figure 18) can be pro-

duced for 30 - 40 M_\odot progenitor stars. Their models are for rotating progenitors; their model CE (CE-3) with $[\text{Fe}/\text{H}] = -3$ for explosion properties calibrated to reproduce the ^{56}Ni - M (progenitor mass) relation inferred from SN observations produces the highest dust mass. Todini & Ferrara (2001) predicted that 30 - 35 M_\odot progenitors produce a factor of 2 - 3 times higher dust masses than 25 M_\odot progenitors and a factor of 4-5 times higher than 12 - 19 M_\odot (SN IIP) progenitors; 30 M_\odot progenitors predominantly produce carbon grains. Marassi et al. (2019) also find that carbon grains dominate with additional Mg_2SiO_4 and MgSiO_3 present for a progenitor of 30 - 50 M_\odot (see Figure 11 of Marassi et al. 2019). N132D may be an example of this.

We examine the dust condensation efficiency for N132D. Figure 18 shows the ejecta mass range is 9.72 - 11.88 M_\odot for a 30 - 40 M_\odot progenitor (Woosley & Weaver 1995). The maximum dust produced (assuming no dust destruction) is 3.03 - 3.59 M_\odot corresponding to a dust condensation efficiency range of 0.28 - 0.3 (Dwek et al. 2007).

Detailed explosion and dust formation models accounting for rotation, different explosion energies, and abundances predict maximum dust masses of between 1.9 and 3.4 M_\odot (Marassi et al. 2019), which corresponds to an efficiency of 0.20 - 0.28 for a 30 - 40 M_\odot progenitor. We also derive dust condensation efficiencies (thick green

line in Figure 18) from the observed dust mass and the ejecta mass from theoretical models depending on the progenitor mass. Using our derived dust mass for N132D ($1.25 \pm 0.65 M_{\odot}$) for a combination of silicate and carbon dust (Model A6 in Table 6), and we estimate the dust condensation efficiency to be 0.10 ± 0.05 using the dust mass divided by the gas mass of $11.88 M_{\odot}$ for a $40 M_{\odot}$ progenitor star (marked as a green curve in Fig. 18). This is a factor of 2 - 3 smaller than efficiencies estimated from theoretical models when assuming no dust destruction (marked as a light green curve in Fig. 18; Dwek et al. 2007).

4.7.2. Dust production rate

We derive a dust productivity (μ_D) defined in Gall et al. (2011) and Dwek et al. (2007) using the stellar initial functions (IMFs; ϕ_m) and the dust mass ($M_d = M_Z \epsilon$ where M_Z is the mass in metals and ϵ is a condensation efficiency). In other words, the dust productivity is the dust production rate per year and per ccSN. The dust productivity (μ_D ; Gall et al. 2011) is given by:

$$\mu_D = \int_{m_l}^{m_u} \phi_m \frac{M_Z}{M_{\odot}} \epsilon(m) dm$$

$$\mu_D (obs) = \int_{m_l}^{m_u} \phi_m M_d (obs) dm$$

The observed dust mass, $M_d(obs)$, is from the four YSNRs, including our estimate for N132D, and the dust-mass yield (see M_{dust} in Figure 18) is estimated from a theoretical model by Dwek et al. (2007). We used the Salpeter and top-heavy IMFs (the total sum of ϕ_m from $m_l = 0.1 M_{\odot}$ to $m_u = 100 M_{\odot}$ is normalized to be 1; Salpeter 1955; Kroupa 2001), which are shown in Figure 19a.

The dust productivities ($\mu_D(obs)$) for the progenitor masses of the four YSNRs are estimated from the observed dust masses and are shown in Figure 19b. The upper limits of μ_D are calculated using the theoretical dust yields (Dwek et al. 2007) where no dust destruction is assumed, and the lower limits are calculated using the observed dust masses of the four YSNRs ($0.39 M_{\odot}$ using carbon dust for N132D). Gall et al. (2011) estimated the dust productivity using the dust observed in QSOs at $z \geq 6$ (Bertoldi et al. 2003). The dust production rate in the early Universe for 400 Myr after the Big Bang is $R_D = M_D/\delta t = 0.5 M_{\odot} \text{ yr}^{-1} = \mu_D \psi$ where ψ ($= 500 - 1500 M_{\odot} \text{ yr}^{-1}$) is the SFR (Bertoldi et al. 2003; Wang et al. 2010). This leads to $\mu_D = 10^{-3}$ ($= 0.5 / 500$), which is the minimum dust productivity, which we call a critical dust productivity ($= \mu_D(crit)$; marked as a dotted line in Fig. 19b), required to explain the dust in the early Universe (see Gall et al. 2011; Dwek et al. 2007, for details).

The dust productivities using the top-heavy IMF are higher than $\mu_D(crit)$. The dust productivities using the Salpeter IMF are higher, but their lower limits are below $\mu_D(crit)$. Dwek & Cherchneff (2011) showed that AGB stars are only minor contributors to the dust abundance in the early Universe. Figure 19b shows that for a top-heavy IMF, the dust productivity (μ_D) is higher than the critical dust productivity ($\mu_D(crit)$). In particular, the implied μ_D from the dust mass of N132D for $40 M_{\odot}$

progenitors is a factor of 5 - 20 higher than the dust productivity required to explain the dust mass in the early Universe. Using a Salpeter IMF, μ_D is higher than $\mu_D(crit)$; however, after accounting for the errors, the lower limit of μ_D is below $\mu_D(crit)$. In summary, the estimated dust productivity implies that the dust from ccSNe can explain the dust observed in the early Universe when we assume a top-heavy IMF.

Our conclusion, based in part on the observations reported here, that dust produced by ccSNe can account for a large amount of dust observed in the early Universe, considers the uncertainties associated with dust survival. The reason is because the dust mass observed in the young SNR N132D is after the dust destruction occurs in reverse shocks that traverse the ejecta. The dust destruction may continue, but molecule reformation in the post-shock gas can reduce the dust destruction (Biscaro & Cherchneff 2014; Matsuura et al. 2019). Early studies suggested that the lifetimes of the major dust materials against destruction are short compared to the time scales for the dust formation (Jones et al. 1996) and imply 45-100% destruction in (Nozawa et al. 2007; Bianchi & Schneider 2007). However, more recent work (Silvia et al. 2012; Nath et al. 2008; Jones & Nuth 2011) indicate lower destruction percentages (1-50%). In addition, hydrodynamical calculations show that up to 20 - 50% of the dust can survive (Slavin et al. 2020). Adding to the uncertainties, dust destruction rates vary depending on dust composition, grain size, and reverse-shock properties. For example, carbon dust is more resilient against the supernova shock than silicate dust (Silvia et al. 2012; Jones & Nuth 2011; Kirchschrager et al. 2019; Priestley et al. 2021; Slavin et al. 2020).

Clearly, N132D alone does not resolve the issue of dust production in the early Universe. Further observational and theoretical work is required. The JWST has recently detected galaxies in the early Universe at $z > 12$ (Pontoppidan et al. 2022; Finkelstein et al. 2022; Treu et al. 2022). The nature of the dust in them and how that dust was produced will be subjects of great interest. The observations reported here of N132D, with its high progenitor mass and high dust mass, raise the possibility that ccSNe associated with high mass progenitors could make a significant contribution to the dust observed in early galaxies, despite their being only a small percentage of the IMF compared to SNe with smaller progenitor masses (e.g., SNe IIP).

JWST can resolve the ejecta and dust continuum structures in N132D on a spatial resolution similar to the HST and may find a direct correlation between them, as *Spitzer* revealed the one-to-one correlation between the Ar ejecta and $21 \mu\text{m}$ -dust in Cas A (Rho et al. 2008). JWST is also important in unambiguously identifying dust features and understanding the dust composition. Most importantly, spectral coverage in far-IR with a higher spatial resolution, such as would be possible with the Origins Space Telescope (Leisawitz et al. 2021), together with JWST, is vital in distinguishing between complex dust models, including multi-composition dust populations, where the shape of the continuum can constrain the composition and yield accurate dust masses. Detailed dust formation models for massive stars

(> 25 M_{\odot}) including SN Type Ib or Ic, and including all dust compositions, are also needed.

CONCLUSIONS

1. We present *Spitzer*, *WISE*, and *Herschel* observations of the young supernova remnant (SNR) N132D in the Large Magellanic Cloud, including 3-40 μm *Spitzer* IRS mapping, 12 μm *WISE* and 70, 100, 160, 250, 350, and 500 μm *Herschel* photometry. The [Ne III] at 15.5 μm and [O IV] 26 μm , and [Si II] 34.8 μm maps reveal a spatial distribution of infrared-emitting ejecta coinciding with the optical and X-ray ejecta at the center and the two CSM/ISM knots of Lasker's Bowl and the West Complex. *WISE* 12 μm image is essentially a [Ne II] map that shows both dominant ejecta emission at the center and shocked ISM emission at the shell.

2. The line width of [Ne III] is larger than the instrumental spectral resolution. The implied velocity is 3167 ± 60 and 3620 ± 47 km s^{-1} for the NE ejecta and central ejecta, respectively.

3. Ejecta spectra of N132D are remarkably similar to those of another YSNR, 1E0102, in the Ne and O lines and continuum shapes. N132D shows a higher ratio of [Ne II]/[Ne III] than 1E0102. Shock modeling of Ne ejecta emission suggests a gas temperature of ~ 500 K and densities in the range $1000 - 3000 \text{ cm}^{-3}$.

4. The Lasker's Bowl and West Complex regions contain dense CSM knots from pre-SN mass loss which emit strong [Fe II]/[S III] emission at 18 μm as well as weaker neon and oxygen emission. They show bright [Fe II], [Ar II], [S III], and [Ni II] lines. Diagnostics of the [Fe II] lines using line ratios 17.9/5.35 μm and 17.9/26 μm imply densities of 2000 - 12000 cm^{-3} of the CSM knots and temperatures of $(6 - 13) \times 10^4$ K.

5. The PACS and SPIRE images of N132D show infrared emission at the center and in the shell. The cold dust at the center coincides with the optical/X-ray/infrared ejecta, implying that there is freshly formed dust there. The continuum from the ejecta shows an 18 μm dust feature.

6. We performed spectral fitting to the IRS dust con-

tinuum and *Herschel* far-IR photometry. The spectra are fitted with the compositions of MgSiO_3 and Mg_2SiO_4 , carbon, and Al_2O_3 . The 18 μm -dust feature requires forsterite grains. The derived dust mass for the ejecta in the central region is $1.25 \pm 0.65 M_{\odot}$ using a combination of cold silicate carbon dust, which implies that the range of possible dust mass is 0.6 - 1.9 M_{\odot} . The dust mass of N132D may be higher than those of other YSNRs and exceed the typical expectations of dust mass per ccSN. This may be due to N132D's high progenitor mass of 30 - 50 M_{\odot} .

7. N132D is suggested to be the result of the explosion of a massive star with a progenitor mass of 30 - 50 M_{\odot} . We estimate the dust condensation efficiency in N132D to be $\sim 11\%$, lower than for lower mass progenitor stars. The dust productivities of N132D and other YSNRs using a top-heavy IMF are higher than the critical dust productivity $\mu_D(\text{crit})$, suggesting that dust from ccSNe could explain the amount of dust present in the early Universe. However, it is necessary to expand the sample of galaxies in the early Universe since the dust productivity depends on the SFR, dust mass measurements, and the evolution time scale. It is also vital to have more samples of nearby ccSNe and YSNRs with different progenitor masses and accurate measurements of their dust masses for more convincing tests of whether ccSNe are the main dust producers in the early Universe.

We thank Felix Priestley for running the DINAMO models and guiding us to run the code, Charles Law and Dan Milisavljevic for providing the velocity map of fast O-rich knots, and Achim Tappe for updating temperature-dependent atomic data of Fe. J.R. would like to thank T. R. Geballe for carefully reading the manuscript and helping to clarify the text. We thank the anonymous referee for insightful and detailed comments. *Herschel* is an ESA space observatory with science instruments provided by European-led Principal Investigator consortia and with important participation from NASA. J.R. and A.P.R. acknowledge support from NASA ADAP grants NNX12AG97G and 80NSSC20K0449.

REFERENCES

- Bautista, M. A. 2004, *A&A*, 420, 763
 Begemann, B., Dorschner, J., Henning, T., et al. 1997, *ApJ*, 476, 199
 Behar, E., Rasmussen, A. P., Griffiths, R. G., et al. 2001, *A&A*, 365, L242
 Bertoldi, F., Carilli, C. L., Cox, P., et al. 2003, *A&A*, 406, L55
 Bianchi, S., & Schneider, R. 2007, *MNRAS*, 378, 973
 Biscaro, C., & Cherchneff, I. 2014, *A&A*, 564, A25
 Blair, W. P., Morse, J. A., Raymond, J. C., et al. 2000, *ApJ*, 537, 667
 Bohren, C. F., & Huffman, D. R. 1985, *Absorption and Scattering of Light by Small Particles*, 571 (New York: Wiley), 571
 Borkowski, K. J., Hendrick, S. P., & Reynolds, S. P. 2007, *ApJ*, 671, L45
 Boulanger, F., Abergel, A., Bernard, J. P., et al. 1996, *A&A*, 312, 256
 Chawner, H., Marsh, K., Matsuura, M., et al. 2019, *MNRAS*, 483, 70
 Dayal, P., Ferrara, A., Sommovigo, L., et al. 2022, *MNRAS*, 512, 989
 De Looze, I., Barlow, M. J., Swinyard, B. M., et al. 2017, *MNRAS*, 465, 3309
 Dickel, J. R., & Milne, D. K. 1995, *AJ*, 109, 200
 Dopita, M. A., Vogt, F. P. A., Sutherland, R. S., et al. 2018, *ApJS*, 237, 10
 Dwek, E., & Cherchneff, I. 2011, *ApJ*, 727, 63
 Dwek, E., Galliano, F., & Jones, A. P. 2007, *ApJ*, 662, 927
 Ferland, G. J., Chatzikos, M., Guzmán, F., et al. 2017, *RMxAA*, 53, 385
 Finkelstein, S. L., Bagley, M. B., Haro, P. A., et al. 2022, *ApJ*, 940, L55
 Foreman-Mackey, D., Hogg, D. W., Lang, D., & Goodman, J. 2013, *PASP*, 125, 306
 France, K., Beasley, M., Keeney, B. A., et al. 2009, *ApJ*, 707, L27
 Gal-Yam, A., Bruch, R., Schulze, S., et al. 2021, *arXiv e-prints*, arXiv:2111.12435
 Galavis, M. E., Mendoza, C., & Zeppen, C. J. 1995, *A&AS*, 111, 347
 Galavis, M. E., Mendoza, C., & Zeppen, C. J. 1998, *A&AS*, 133, 245
 Gall, C., Hjorth, J., & Andersen, A. C. 2011, *A&A Rev.*, 19, 43
 Gomez, H. L., Krause, O., Barlow, M. J., et al. 2012, *ApJ*, 760, 96
 Guest, B. T., Safi-Harb, S., & Tang, X. 2019, *MNRAS*, 482, 1031
 Hartigan, P., Raymond, J., & Hartmann, L. 1987, *ApJ*, 316, 323
 Hewitt, J. W., Rho, J., Andersen, M., & Reach, W. T. 2009, *ApJ*, 694, 1266

- Houck, J. R., Roellig, T. L., van Cleve, J., et al. 2004, *ApJS*, 154, 18
- Hwang, U., Hughes, J. P., Canizares, C. R., & Markert, T. H. 1993, *ApJ*, 414, 219
- Indebetouw, R., Matsuura, M., Dwek, E., et al. 2014, *ApJ*, 782, L2
- Isaak, K. G., Priddey, R. S., McMahon, R. G., et al. 2002, *MNRAS*, 329, 149
- Jones, A. P., & Nuth, J. A. 2011, *A&A*, 530, A44
- Jones, A. P., Tielens, A. G. G. M., & Hollenbach, D. J. 1996, *ApJ*, 469, 740
- Kirchschlager, F., Schmidt, F. D., Barlow, M. J., et al. 2019, *MNRAS*, 489, 4465
- Kotak, R., Meikle, P., Pozzo, M., et al. 2006, *ApJ*, 651, L117
- Kroupa, P. 2001, *MNRAS*, 322, 231
- Lagache, G., Abergel, A., Boulanger, F., & Puget, J. L. 1998, *A&A*, 333, 709
- Lai, T. S. Y., Smith, J. D. T., Baba, S., Spoon, H. W. W., & Imanishi, M. 2020, *ApJ*, 905, 55
- Laporte, N., Ellis, R. S., Boone, F., et al. 2017, *ApJ*, 837, L21
- Lasker, B. M. 1980, *ApJ*, 237, 765
- Law, C. J., Milisavljevic, D., Patnaude, D. J., et al. 2020, *ApJ*, 894, 73
- Leisawitz, D., Amatuucci, E., Allen, L., et al. 2021, *Journal of Astronomical Telescopes, Instruments, and Systems*, 7, 011014
- Marassi, S., Schneider, R., Limongi, M., et al. 2019, *MNRAS*, 484, 2587
- Markwardt, C. B. 2009, in *Astronomical Society of the Pacific Conference Series*, Vol. 411, *Astronomical Data Analysis Software and Systems XVIII*, ed. D. A. Bohlender, D. Durand, & P. Dowler, 251
- Matsuura, M., Dwek, E., Meixner, M., et al. 2011, *Science*, 333, 1258
- Matsuura, M., Dwek, E., Barlow, M. J., et al. 2015, *ApJ*, 800, 50
- Matsuura, M., De Buizer, J. M., Arendt, R. G., et al. 2019, *MNRAS*, 482, 1715
- Michalowski, M. J. 2015, *A&A*, 577, A80
- Millard, M. J., Ravi, A. P., Rho, J., & Park, S. 2021, *ApJS*, 257, 36
- Morgan, H. L., & Edmunds, M. G. 2003, *MNRAS*, 343, 427
- Morse, J. A., Winkler, P. F., & Kirshner, R. P. 1995, *AJ*, 109, 2104
- Morse, J. A., Blair, W. P., Dopita, M. A., et al. 1996, *AJ*, 112, 509
- Nath, B. B., Laskar, T., & Shull, J. M. 2008, *ApJ*, 682, 1055
- Nozawa, T., Kozasa, T., Habe, A., et al. 2007, *ApJ*, 666, 955
- Nozawa, T., Kozasa, T., Umeda, H., Maeda, K., & Nomoto, K. 2003, *ApJ*, 598, 785
- Nozawa, T., Kozasa, T., Tominaga, N., et al. 2008, *ApJ*, 684, 1343
- Owen, P. J., & Barlow, M. J. 2015, *ApJ*, 801, 141
- Poglitsch, A., Waelkens, C., Geis, N., et al. 2010, *A&A*, 518, L2
- Pontoppidan, K. M., Barrientes, J., Blome, C., et al. 2022, *ApJ*, 936, L14
- Priestley, F. D., Arias, M., Barlow, M. J., & De Looze, I. 2022, *MNRAS*, 509, 3163
- Priestley, F. D., Barlow, M. J., & De Looze, I. 2019, *MNRAS*, 485, 440
- Priestley, F. D., Chawner, H., Matsuura, M., et al. 2021, *MNRAS*, 500, 2543
- Ramsbottom, C. A., Hudson, C. E., Norrington, P. H., & Scott, M. P. 2007, *A&A*, 475, 765
- Reach, W. T., & Rho, J. 2000, *ApJ*, 544, 843
- Reach, W. T., Dwek, E., Fixsen, D. J., et al. 1995, *ApJ*, 451, 188
- Rho, J., Jarrett, T. H., Cutri, R. M., & Reach, W. T. 2001, *ApJ*, 547, 885
- Rho, J., Reach, W. T., Tappe, A., et al. 2009, *ApJ*, 700, 579
- Rho, J., Kozasa, T., Reach, W. T., et al. 2008, *ApJ*, 673, 271
- Rho, J., Gomez, H. L., Boogert, A., et al. 2018, *MNRAS*, 479, 5101
- Salpeter, E. E. 1955, *ApJ*, 121, 161
- Sano, H., Plucinsky, P. P., Bamba, A., et al. 2020, *ApJ*, 902, 53
- Sarangi, A., & Cherchneff, I. 2015, *A&A*, 575, A95
- Sharda, P., Gaetz, T. J., Kashyap, V. L., & Plucinsky, P. P. 2020, *ApJ*, 894, 145
- Shull, J. M., & McKee, C. F. 1979, *ApJ*, 227, 131
- Siegel, J., Dwarkadas, V. V., Frank, K. A., & Burrows, D. N. 2021, *arXiv e-prints*, arXiv:2109.01157
- Silvia, D. W., Smith, B. D., & Shull, J. M. 2012, *ApJ*, 748, 12
- Slavin, J. D., Dwek, E., Mac Low, M.-M., & Hill, A. S. 2020, *ApJ*, 902, 135
- Sluder, A., Milosavljević, M., & Montgomery, M. H. 2018, *MNRAS*, 480, 5580
- Smith, J. D. T., Draine, B. T., Dale, D. A., et al. 2007, *ApJ*, 656, 770
- Sommovigo, L., Ferrara, A., Pallottini, A., et al. 2022, *MNRAS*, arXiv:2202.01227
- Spilker, J. S., Aravena, M., Béthermin, M., et al. 2018, *Science*, 361, 1016
- Sutherland, R. S., Bicknell, G. V., & Dopita, M. A. 1993, *ApJ*, 414, 510
- Sutherland, R. S., & Dopita, M. A. 1995, *ApJ*, 439, 381
- Swinyard, B. M., Ade, P., Baluteau, J. P., et al. 2010, *A&A*, 518, L4
- Tacchella, S., Finkelstein, S. L., Bagley, M., et al. 2022, *ApJ*, 927, 170
- Tappe, A., Rho, J., Boersma, C., & Micelotta, E. R. 2012, *ApJ*, 754, 132
- Tappe, A., Rho, J., & Reach, W. T. 2006, *ApJ*, 653, 267
- Temim, T., Dwek, E., Arendt, R. G., et al. 2017, *ApJ*, 836, 129
- Temim, T., Sonneborn, G., Dwek, E., et al. 2012, *ApJ*, 753, 72
- Todini, P., & Ferrara, A. 2001, *MNRAS*, 325, 726
- Treu, T., Roberts-Borsani, G., Bradac, M., et al. 2022, *ApJ*, 935, 110
- Vogt, F., & Dopita, M. A. 2011, *Ap&SS*, 331, 521
- Wang, R., Carilli, C. L., Neri, R., et al. 2010, *ApJ*, 714, 699
- Woosley, S. E., & Weaver, T. A. 1995, *ApJS*, 101, 181
- Wright, E. L., Eisenhardt, P. R. M., Mainzer, A. K., et al. 2010, *AJ*, 140, 1868